REMTES
TECHNOLOGY FOR REMOTE TEMPERATURE
MEASUREMENTS IN MICROFLUIDIC DEVICES

PROGRAM-PRIZMA-2023-2026
Grant Agreement: 7017

Deliverable 1.1

Ln^{3+}- and TM-doped luminescence

thermal probes

Version Final

Project Deliverable Information Sheet

REMTES Project	Project Ref. No. 7017
	Project Title: Technology for remote temperature measurements in microfluidic devices
	Project Website: https://www.remtes-prizma.org
	Deliverable No.: D 1.1
	Deliverable Type: Report
	Month of delivery: 12
	Actual Delivery Date: 30/11/2024
	Principal investigator: Miroslav DRAMIĆANIN

Document Control Sheet

Document	Title: Ln³⁺- and TM-doped luminescence thermal probes.docx
	Version Final
	Distributed to REMTES Participants and through Project Website
Authorship	Written by Željka Antić
	Contributed by Tatjana Dramićanin, Sanja Kuzman, Ljubica Đačanin Far, Katarina Milenković
	Reviewed by Miroslav Dramićanin
	Approved by Miroslav Dramićanin

History of Changes

Version	Date	Description	Reviewer
V0	01.11.2024.	Version 0	Željka Antić
V1	20.11.2024.	Version 1	Tatjana Dramićanin, Sanja Kuzman, Ljubica Đačanin Far, Katarina Milenković
V2	30.11.2024.	Version Final	Miroslav Dramićanin

Table of Contents

INTRODUCTION

REMTES – "Technology for remote temperature measurements in microfluidic devices" is a Science Fund of the Republic of Serbia funded project (Program PRIZMA, Grant Contract No. 7017) coordinated and completely executed by "Vinča" Institute of Nuclear Sciences – National Institute of the Republic of Serbia, University of Belgrade (VINS). The project will run from December 1st 2023 to November 30th 2026.

REMTES is a highly ambitious and innovative project aimed at developing a breakthrough system for measuring sample temperatures on the nanoliter scale. The project will develop an optical self-referencing thermometer for use in micro- and nanofluidics in the 0–100 °C temperature range by exploiting temperature-induced changes in the luminescence of materials and nanomaterials; that is, by advancing luminescence (nano-) thermometry in a targeted manner. The project aims to go beyond the state of the art and implement a radically new technology that merges the fields of luminescence thermometry, photothermal spectroscopy, and microfluidics to develop new-generation luminescent thermometry probes using cutting-edge luminescent, temperature-sensitive, and chemically stable inorganic materials in bulk and nanomaterial forms. The probes will be embedded in microfluidic chip channels to enable self-referenced remote temperature measurements, and the technology will be validated by a portable microfluidic luminescent thermometer, as well as in-situ temperature measurements of fluid flow in nanoliter volume samples. Multiple conceptual breakthroughs can be further envisaged from the proposed technology credibly spreading its impact to multiple technological areas.

The present document – **D.1.1 Ln^{3+}- and TM-doped luminescence thermal probes** is a deliverable of the W1 of the REMTES project. The report describes Ln^{3+} and TM-doped luminescence thermal probes, with their basic structural, morphological, and luminescence features. This report is the result of a joint effort between WP1, WP2, and WP3. Up to four probes are selected for further implementation in a microfluidic device with integrated luminescence thermometers.

D 1.1. Ln^{3+}- and TM-DOPED LUMINESCENCE THERMAL PROBES

Starting from the project beginning up to the end of the first project year, REMTES team members under SUBACTIVITY 1.1: LANTHANIDE-ACTIVATED INORGANIC LUMINESCENCE THERMAL PROBES; SUBACTIVITY 1.2: TRANSITION METAL ACTIVATED INORGANIC LUMINESCENCE THERMAL PROBES; SUBACTIVITY 2.1: STRUCTURAL, MORPHOLOGICAL, AND THERMAL PROPERTIES OF LUMINESCENT PROBES and SUBACTIVITY 3.1: MICROSCOPIC MODELLING OF LUMINESCENT PROCESSES designed, synthesized and structurally, morphologically and optically characterized various Ln^{3+}- and TM-doped luminescence thermal probes. Properties of thermal probes based on Eu^{3+}-doped CsY_2F_7 and RbY_2F_7; Pr^{3+}-doped YF_3 and Eu^{3+}-doped $Y_2Mo_3O_{12}$ were reported and published in:

1. K. Milenković, I. Zeković, B. Milićević, Z. Ristić, K. Smits, A. Popov, M.D Dramićanin, V. Đorđević, Microwave-assisted solvothermal synthesis of Eu3+-doped CsY_2F_7 and RbY_2F_7 phosphorescent nanoparticles, Ceramics International, 50 (15), 26663-26669, 2024, https://doi.org/10.1016/j.ceramint.2024.04.394 (*Subscription*).

2. A. Rajčić, Z. Ristić, J. Periša, B. Milićević, S. Aldawood, A.N. Alodhay, Ž. Antić, M.D. Dramićanin, Using Principal Component Analysis for Temperature Readings from YF_3:Pr^{3+} Luminescence, Technologies, 12(8), 131, 2024, https://doi.org/10.3390/technologies12080131 (*Open Access*).

3. T. Gavrilović, A. Ćirić, M. Medić, Z. Ristić, J. Periša, Ž. Antić, M.D. Dramićanin, Structure–Dopant Concentration Relations in Europium-Doped Yttrium Molybdate and Peak-Sharpening for Luminescence Temperature Sensing, Materials, 17 (17), 4267, 2024, https://doi.org/10.3390/ma17174267 (*Open Access*).

4. T. Gavrilović, V. Đorđević, J. Periša, M. Medić, Z. Ristić, A. Ćirić, Ž. Antić, M.D. Dramićanin,, Luminescence Thermometry with Eu^{3+}-Doped $Y_2Mo_3O_{12}$: Comparison of Performance of Intensity Ratio and Machine Learning Temperature Read-Outs, Materials, 17 (21), 5354, 2024, https://doi.org/10.3390/ma17215354 (*Open Access*).

Three, out of four publications were published in an Open Access form.

Besides the reported probes and from the activities within the subactivities, REMTES team members reached *Milestone M1.1 - A list of Ln and TM-activated hosts for the superior thermometric performance of luminescence probes obtained by theoretical modeling and experimental data* to be used further for the development of a microfluidic luminescent probe. The list is as follows:

1. Eu^{3+} - doped Sr_2GdF_7 colloidal nanoparticles

2. Mn^{5+}-doped $Ca_6Ba(PO_4)_4O$ powders

3. Er^{3+} and Er^{3+}/Yb^{3+} doped $LaPO_4$ colloidal nanoparticles

4. Er^{3+}, Nd^{3+} and Tm^{3+}-doped YVO_4 colloidal nanoparticles

Eu^{3+} - doped Sr$_2$GdF$_7$ colloidal nanoparticles

Synthesis: The hydrothermal method was used to prepare a set of seven Sr$_2$Gd$_{1-x}$Eu$_x$F$_7$ (x = 0, 0.05, 0.10, 0.40, 0.60. 0.80, and 1.00, where mol.% of Eu^{3+} dopant ions were added with respect to Gd^{3+}) colloids, as illustrated in Figure 1. A typical synthesis procedure includes metal nitrates and NH$_4$F as precursors and EDTA-2Na as a stabilizing agent [1]. Due to the ability to improve crystalline seed dispersibility by forming [Sr-EDTA]$^{2+}$ and [Gd-EDTA]$^+$ complexes after mixing all the chemicals, EDTA-2Na prevented SGF particle aggregation during the subsequent hydrothermal treatment. At the same time, [Gd-EDTA]$^+$ cations are adsorbed on the surfaces of SGF particles, additionally improving their stability. Typically, for the synthesis, all nitrates were weighed according to the stoichiometric ratio and dissolved in 12.5 ml of deionized water while stirring at room temperature. The solutions were mixed for 30 min with a transparent solution of EDTA-2Na in 12.5 ml of water (molar ratio EDTA-2Na : Ln = 1:1). Following that, 10 ml of NH$_4$F aqueous solution (molar ratio NH$_4$F : Ln = 12:1) was added and vigorously stirred for 1 h, yielding a white suspension. The pH value of the mixture was adjusted to around 6 using NH$_4$OH. Hydrothermal treatment was carried out in a 100-ml Teflon-lined autoclave in the oven at 180 °C for 20 h followed by natural cooling. Obtained colloidal suspensions were acidic with pH = 6. The described method produced undoped SGF and SGF phosphors with varying concentrations of Eu^{3+} ions. The colloidal suspensions were dried in the air, and obtained powders used for XRD analysis, diffuse reflectance, and temperature-dependent photoluminescent measurements. The amounts of precursors used for synthesizing ~0.0025 mol (~1.2 g) of samples are given in Table 1.
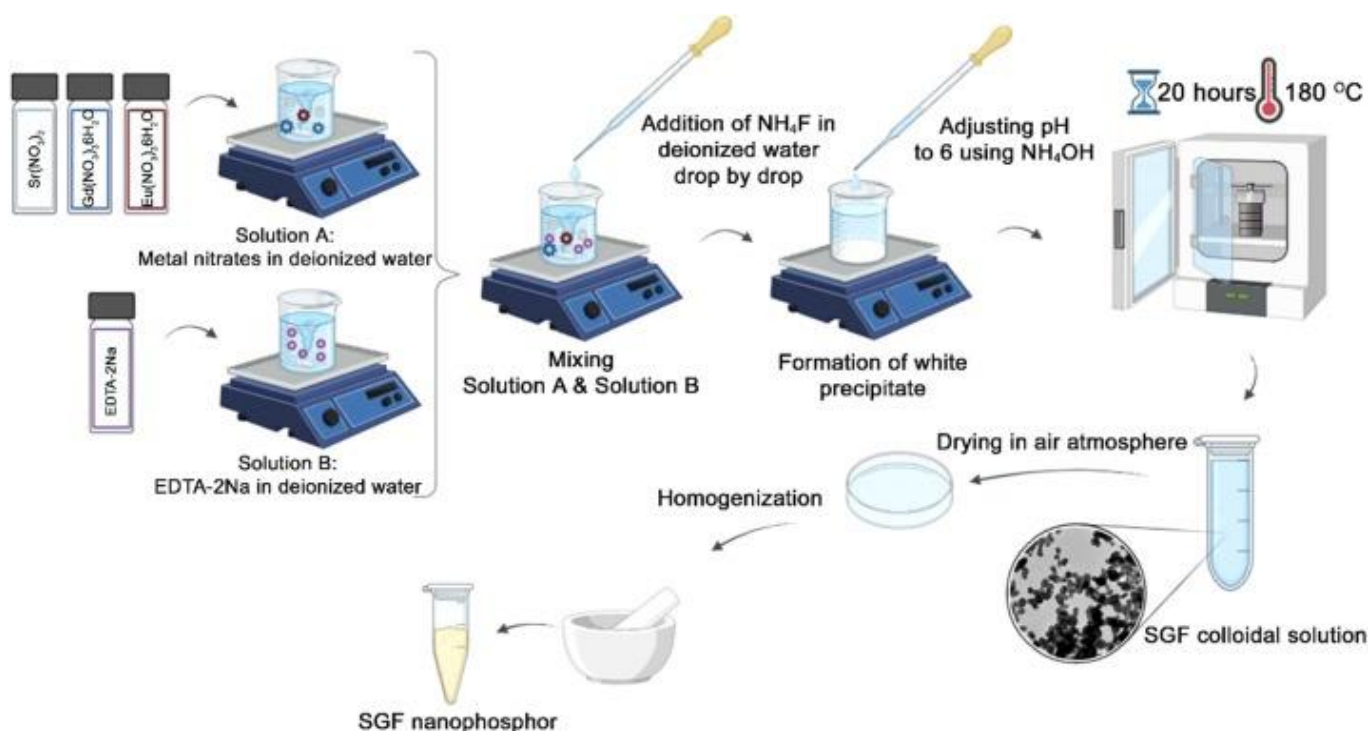

Figure 1. Schematic illustration of the colloidal and powder SGF:Eu nanophosphors preparation.

Table 1. The amounts of precursors needed for synthesizing 0.0025 mol of samples.

	Sr(NO₃)₂ (g)	Gd(NO₃)₃·6H₂O (g)	Eu(NO₃)₃·6H₂O (g)	NH₄F (g)	EDTA (g)
SGF	1.0582	1.1284	/	1.1111	0.9306
SGF_5Eu	1.0582	1.0720	0.0557	1.1111	0.9306
SGF_10Eu	1.0582	1.0156	0.1115	1.1111	0.9306
SGF_40Eu	1.0582	0.6770	0.4460	1.1111	0.9306
SGF_60Eu	1.0582	0.4514	0.6690	1.1111	0.9306
SGF_80Eu	1.0582	0.2257	0.8919	1.1111	0.9306
SEF	1.0582	/	0.9306	1.1111	0.9306

Structural and morphological characterization: Powder X-ray diffraction (PXRD) patterns of $Sr_2Gd_{1-x}Eu_xF_7$ (x = 0, 0.05, 0.10, 0.40, 0.60. 0.80, and 1.00) nanophosphors are shown in Figure 2a, with Rietveld refinement fits for the two end members, Sr_2GdF_7 (SGF) and Sr_2EuF_7 (SEF), given as Figure 2b-c (R_{wp} = 2.72 % and 3.43 %, respectively). The patterns of Sr_2GdF_7 and Sr_2EuF_7 were fitted using a structural model in the cubic space group $Fm\bar{3}m$ (225), with Sr and Gd ions on Wyckoff site 4a with m-3m symmetry and F ions on Wyckoff site 8c with −43 m symmetry. While in the ideal fluorite-type compound of MX_2 stoichiometry the cations are found in 8-coordinate cubic environments and the anions in 4-coordinate tetrahedral environments, the partial occupancies of both cation and anion sites in Sr_2GdF_7 and Sr_2EuF_7 result in deviations from these ideal coordination geometries and a range of environments is expected to exist for the species present. The unit cell parameters obtained were 5.7484(1) Å for SGF and 5.7618(1) Å for SEF. All observed reflections were accounted for in PXRD patterns of all samples, and the absence of extra peaks confirms the phase purity of the materials prepared. Due to smaller ionic radii of Gd^{3+} (GdVIII3+ = 1.053 Å, [2]) incorporation of larger Eu^{3+} (EuVIII3+ = 1.066 Å, [2]) ions resulted in shifting of diffraction peaks to lower Bragg angles, consistent with the unit cell parameters obtained for the two end members (see Figure 2d).

Transmission electron microscopy (TEM) images of representative colloidal SGF_40 %Eu^{3+} particles, obtained with different magnifications, are shown in Figure 2e-f. Nanoparticles show a similar quasi-spherical shape with the average particle size estimated to be 24 ± 2 nm (see the histogram fitted with a log-normal distribution, based on around 200 particles, Figure 2e inset).
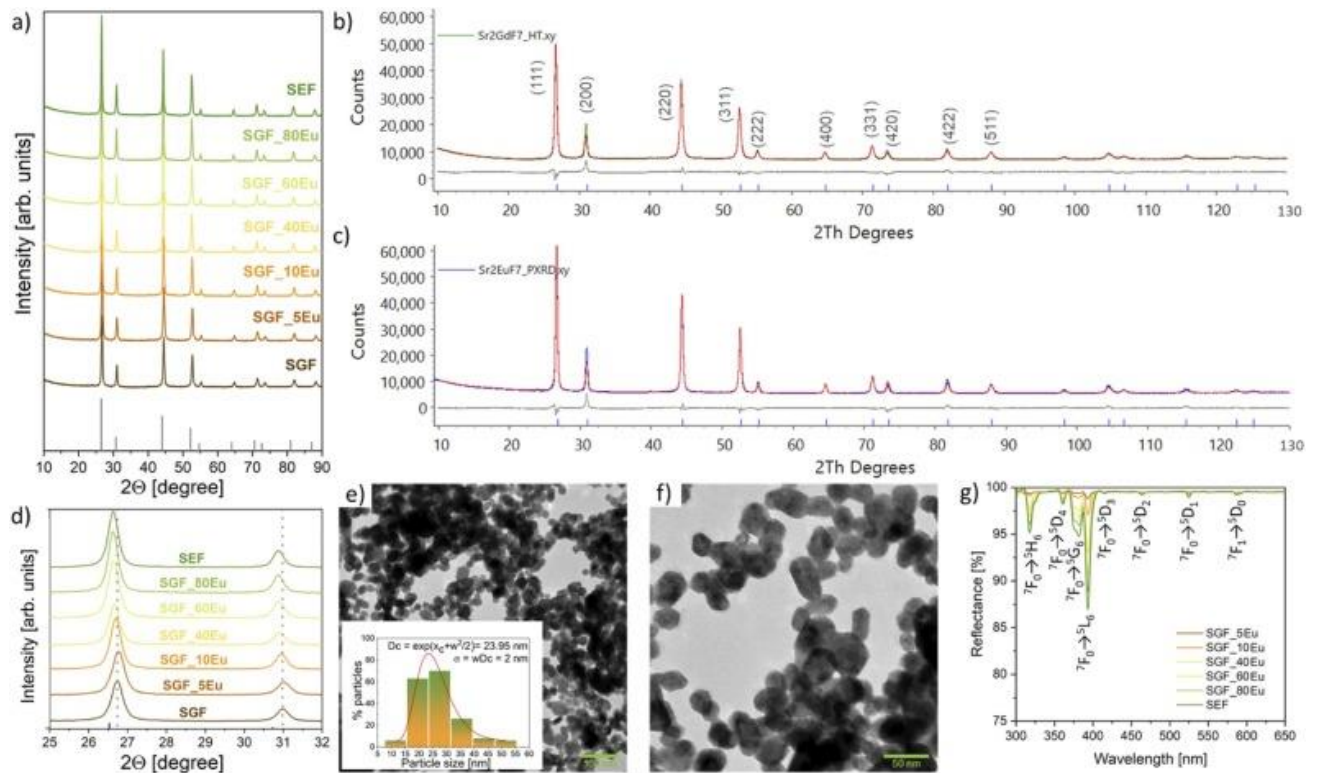
Figure 2. (a) XRD patterns of $Sr_2Gd_{1-x}Eu_xF_7$ (x = 0.05, 0.10, 0.40, 0.60. 0.80, and 1.00) nanophosphors; (b, c) Rietveld fits for Sr_2GdF_7 and Sr_2EuF_7. Green (SGF) and blue (SEF) curves represent the observed pattern, in each case, the red curves are the calculated patterns, and the difference curves are shown in grey, while blue tick marks represent the positions of the Bragg peaks; (d) Enlarged (111) and (200) diffraction peaks showing a shift toward lower Bragg angels due to the replacement of Gd with Eu ions in the host material; (e, f) TEM images under different magnification with the particle size distribution of representative colloidal SGF:40 mol% Eu^{3+} given as Inset in Figure 2e; (g) Room temperature diffuse reflectance spectra for all $Sr_2Gd_{1-x}Eu_xF_7$ (x = 0.05, 0.10, 0.40, 0.60. 0.80, and 1.00) samples.

Optical UV-VIS and photoluminescent characterization: Figure 2g shows the room temperature diffuse reflectance spectra of $Sr_2Gd_{1-x}Eu_xF_7$ (x = 0, 0.05, 0.10, 0.40, 0.60. 0.80, and 1.00) samples in the 300–650 nm wavelength range, which display typical optical features of Eu^{3+} ions [3]. The absorption peaks of Eu^{3+} ions, which are located at 317, 360, 381, 394, 414, 464, 525, and 587 nm correspond to the following electronic transitions: $^7F_0 \rightarrow {}^5H_3$, $^7F_0 \rightarrow {}^5D_4$, $^7F_0 \rightarrow {}^5G_6$, $^7F_0 \rightarrow {}^5L_6$, $^7F_0 \rightarrow {}^5D_3$, $^7F_0 \rightarrow {}^5D_2$, $^7F_0 \rightarrow {}^5D_1$, and $^7F_1 \rightarrow {}^5D_0$, respectively, with the highest absorption at around 394 nm.

The room temperature photoluminescence excitation spectra of all $Sr_2Gd_{1-x}Eu_xF_7$ colloids recorded in the 250–330 nm (λ_{em} = 698 nm) and 310–570 nm (λ_{em} = 593 nm) ranges are given in Figure 3a-b, showing lines that correspond to transitions within the $4f^6$ configuration of Eu^{3+} and $4f^7$ configuration of Gd^{3+}. Emissions centered around 273 and 311 nm (inset in Figure 3b) correspond to Gd^{3+} absorption. The intensity of Gd^{3+} emissions is the largest for the $Sr_2Gd_{0.9}Eu_{0.1}F_7$ composition (90 mol% of Gd^{3+} and 10 mol% of Eu^{3+}), indicating the optimal Eu/Gd ratio for energy transfer from Gd^{3+} to Eu^{3+}.

Photoluminescence emission spectra of all $Sr_2Gd_{1-x}Eu_xF_7$ colloids recorded at room temperature are given in Figure 3c (λ_{ex} = 273 nm) and Figure3d (λ_{ex} = 394 nm). Emission centered at 311 nm, presented in Figure 3c, corresponds to the $^6P_J \rightarrow {}^8S_{7/2}$ transition of Gd^{3+}, while those at longer wavelengths correspond to $4f–4f$ transitions of Eu^{3+}(Figure 3d) placed at ~592 nm ($^5D_0 \rightarrow {}^7F_1$), ~613 nm ($^5D_0 \rightarrow {}^7F_2$), ~650 nm ($^5D_0 \rightarrow {}^7F_3$), and ~700 nm ($^5D_0 \rightarrow {}^7F_4$). Emission peaks from $^5D_1$, $^5D_2$, and $^5D_3$ levels (Figure 3d inset) are the most intense with 10 mol% of Eu^{3+} because of earlier concentration quenching of energetically higher Eu^{3+} levels [4].

The $^5D_0 \rightarrow {}^7F_1$ is a magnetic-dipole transition that does not depend on the local environment.

However, the $^5D_0 \rightarrow {}^7F_2$ electric-dipole transition is a hypersensitive one, and it is highly dependent on changes in the local environment around the Eu^{3+} ions. Theoretically, when the Eu^{3+} ions occupy centrosymmetric sites, the emission spectrum shows a more intense $^5D_0 \rightarrow {}^7F_1$ transition than the $^5D_0 \rightarrow {}^7F_2$ one. This agrees with our experimental observations. In addition, the ratio of the integrated intensity of the $^5D_0 \rightarrow {}^7F_2$ and $^5D_0 \rightarrow {}^7F_1$ transitions, known as the asymmetry ratio, can be considered indicative of the reduction of symmetry of the coordination environment around the Eu^{3+} ion, and is given by eq. (1):

$$R = \frac{I\left({}^5D_0 \rightarrow {}^7F_2\right)}{I\left({}^5D_0 \rightarrow {}^7F_1\right)}. \tag{1}$$

The asymmetry ratio values obtained from the emission spectra do not vary significantly as a function of Eu^{3+} concentration, as shown in Figure 3e. Therefore, one may conclude that the degree of distortion of the local symmetry around Eu^{3+} is similar in the samples in the series produced. This is consistent with the samples being isostructural, as shown by PXRD and Rietveld analysis.

Emission in the deep-red spectral region around 700 nm, which corresponds to the $^5D_0 \rightarrow {}^7F_4$ transition, exhibits high intensity, even higher than emission from $^5D_0 \rightarrow {}^7F_1$ and $^5D_0 \rightarrow {}^7F_2$ transitions. This is not common for Eu^{3+} and it was previously reported for several fluoride hosts where the structural distortion from the octahedral symmetry to the non-centrosymmetric D_{4d} occurs [5,6], as the odd-rank components of the static forced electric dipole and ligand polarizability-dependent dynamic coupling mechanisms are high, especially in the highly polarizable chemical environment [7]. This observation in our spectra is consistent with a range of Eu^{3+} environments present and the breaking of the centrosymmetric m-3m symmetry of the average long-range crystallographic model at a local level, due to the partial site occupancies. Figure 3f shows that photoluminescent intensity continually increases as the Eu^{3+} content increases from 5 mol% to 80 mol%, without concentration quenching. To evaluate real application potential, the absolute photoluminescent quantum efficiency was measured at room temperature with an integrating sphere, and the results are shown in Figure 3f. Efficiency increases with Eu^{3+}-dopant concentration starting from 7% for the 5 mol% doped sample and reaching 60% for the 80% doped sample.

Figure 3g displays the photoluminescent lifetime decay curves of the $Sr_2Gd_{1-x}Eu_xF_7$ ($x = 0.05$, 0.10, 0.40, 0.60. 0.80, and 1.00) colloids recorded at room temperature. To obtain the value of the lifetime (τ), acquired data were fitted to a simple single exponential function:

$$I(t) = I_0 e^{-\frac{t}{\tau}}, \tag{2}$$

where $I(t)$ represents the corresponding emission intensity at time t, I_0 represents the initial emission intensity, and τ represents the emission decay constant (excited state lifetime). As the Eu^{3+} concentration increased, the $^5D_0$-level lifetime gradually decreased from 12.0 to 6.9 ms. The shortening of the lifetime with increasing concentration indicates the activation of concentration-quenching mechanisms. These quenching mechanisms compete with an increase in emission intensity due to an increase in the number of optically active centers when Eu^{3+} concentration is increased, resulting in an intensity net rise with concentrations up to 80% of Eu^{3+} content.

Chromaticity coordinates (x,y) on the CIE chromaticity diagram, a two-dimensional color space that describes all the colors observed by the human eye, can be used to quantify apparent color. We derived the CIE chromaticity coordinates from the photoluminescent spectra to evaluate the color of the synthesized samples, as shown in Figure 3h. For all the samples, CIE coordinates are almost identical (x = 0.62, y = 0.38; λ_{dom} = 598 nm; color purity = 99.1%) and placed in the orange-red portion of the diagram, confirming that there is no significant change in the local symmetry

around Eu³⁺ across the series and consequently in the emission spectra. Figure 3i shows the translucent white color of colloids under daylight and the red appearance of colloids under UV light.
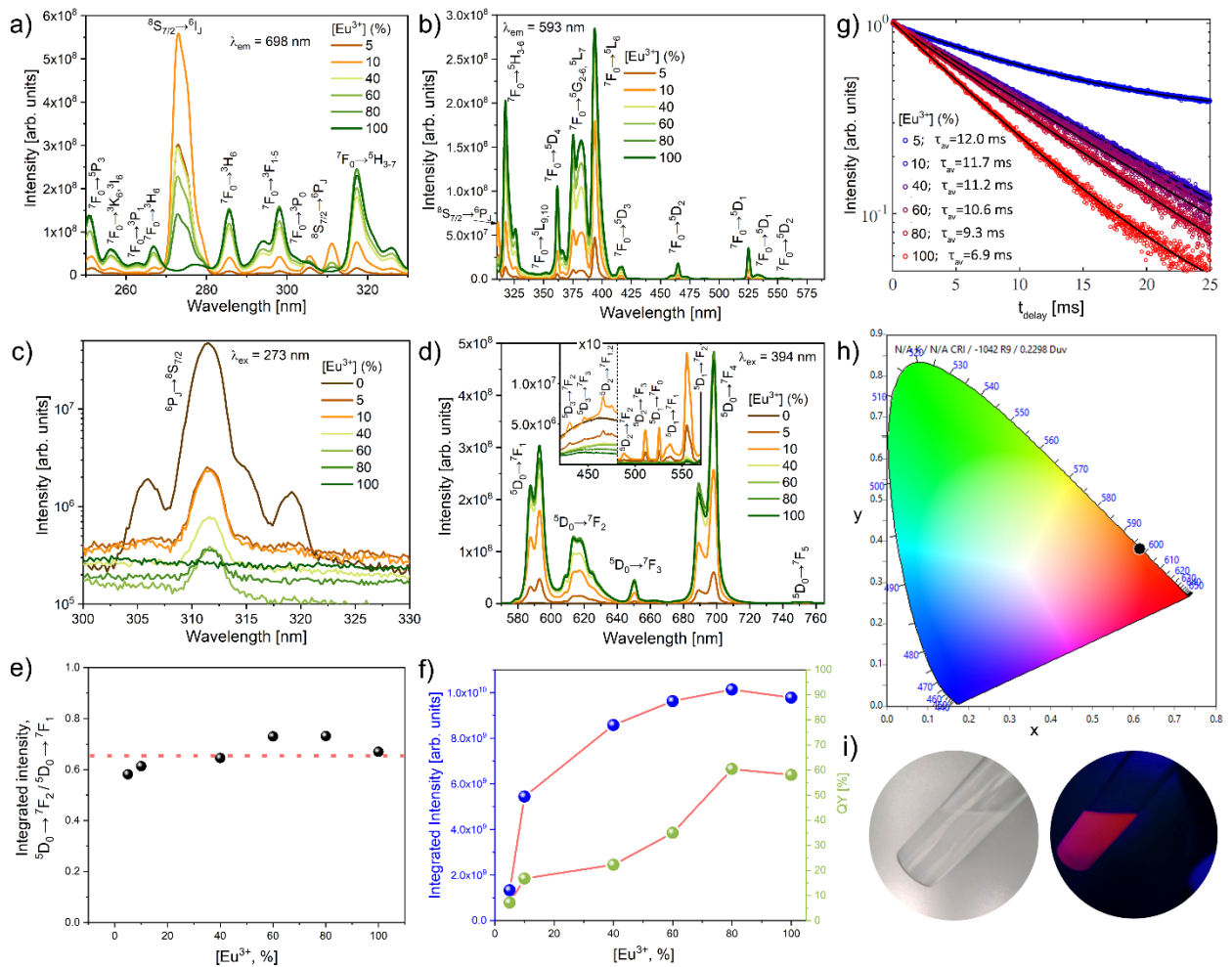
Figure 3 Room temperature photoluminescence of $Sr_2Gd_{1-x}Eu_xF_7$ ($x = 0.05$, 0.10, 0.40, 0.60, 0.80, and 1.00) colloids: a) excitation spectra under $\lambda_{em} = 698$ nm; b) excitation spectra under $\lambda_{em} = 593$ nm; c) emission spectra under $\lambda_{ex} = 273$ nm; d) emission spectra under $\lambda_{ex} = 394$ nm; e) asymmetry ratio as a function of Eu ions concentration; f) integrated emission intensity as a function of Eu ions concentration; g) lifetime decay curves as a function of Eu ions concentration; h) CIE diagram with calculated coordinates; and i) appearance of colloid under daylight and near UV light.

To determine the temperature stability, temperature-dependent photoluminescence measurements in steady-state and time- domains were recorded in the 25–200 °C temperature range on dried samples in powder form. Figure 4a shows the white color of powders under daylight and the red appearance under UV light, which becomes more intense as Eu³⁺ concentration increases. Figure 4b shows the lifetime, while Figure 4c shows the emission intensity as a function of temperature for two representative samples, SGF_5Eu (with the lowest Eu³⁺ content in the series) and SGF_80Eu sample, with the highest emission intensity. For both samples, lifetime values show high-temperature stability in the temperature range relevant for LEDs, while emission intensity shows a slight decrease in the same range. It is important to note that, depending on the manufacturer, 100°C is usually considered the maximal operating temperature of LEDs [8,9], while temperature stability up to 150°C is frequently given in the literature [10]. For SGF_80Eu, the sample with the highest emission intensity, the lifetime, and the emission intensity at 100°C remain at 95% and 83% of their initial values at room temperature, respectively.
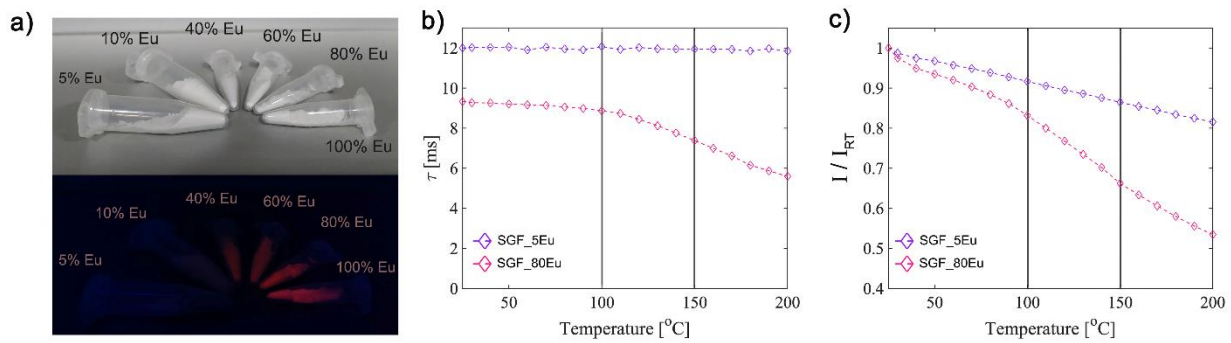
Figure 4 a) Appearance of nanopowders under daylight and near UV light. Temperature-dependence of b) lifetime and c) emission intensity for the whole set of nanopowders.

Judd-Ofelt analysis. The quantum mechanical, semi-empirical, Judd-Ofelt theory [11,12], introduced in the 1960s, presents a centerpiece in lanthanide spectroscopy [13], as the only theory that can explain and predict radiative properties of intra-configurational luminescence in ions from Pr^{3+} to Tm^{3+}. From only three intensity parameters, the theory provides an estimate of the radiative transition probabilities, radiative lifetimes, branching ratios, and cross-sections. It can also give us quantitative information on the non-radiative de-excitation process and intrinsic quantum efficiency if coupled with time-resolved luminescence measurements [14]. The main difficulty in applying the Judd-Ofelt theory is estimating the intensity parameters, Ω_λ, which is usually performed by fitting the intensities in the absorption spectrum to theoretical relations [15].

Europium is a unique ion among lanthanides as it has pure magnetic dipole transitions [16]. Magnetic dipole transitions, unaffected by the host matrix, can be used for calibrating the emission spectrum [17]. Thus, in Eu^{3+} doped materials only a single emission spectrum is sufficient for Judd-Ofelt parametrization, by using the equation [14]:

$$\Omega_\lambda = \frac{D_1}{e^2 U^\lambda} \left(\frac{\bar{\lambda}_\lambda}{\bar{\lambda}_1}\right)^3 \frac{9n_1^3}{n_\lambda (n_\lambda^2 + 2)^2} \frac{I_\lambda}{I_1}, \qquad \lambda = 2,4,6 \tag{3}$$

where e is the elementary charge, D_1 is the magnetic dipole strength, U^λ are the tabulated values of the squared reduced matrix elements, and n is the refractive index. Transition $^5D_0 \rightarrow {}^7F_1$ is denoted with 1 in the subscript, while induced electric-dipole emissions $^5D_0 \rightarrow {}^7F_{\lambda=2,4,6}$ are denoted with $\lambda=2,4,6$ in the subscript. $I_{1,\lambda}$ are the integrated intensities of corresponding emissions.

The asymmetry ratio, a quantitative measure that shows the degree of deviation from the ideal site symmetry of Eu^{3+} ion in the host matrix, given by the ratio of integrated intensities of $^5D_0 \rightarrow {}^7F_2$ to $^5D_0 \rightarrow {}^7F_1$ emission, is directly proportional to the Ω_2 parameter [18]:

$$R = \frac{I_2}{I_1} \propto \Omega_2 \tag{4}$$

The $^5D_0 \rightarrow {}^7F_6$ emission is of very low intensity and usually lies beyond the sensitive spectral range of most detectors. Thus, this part is most frequently neglected in the Judd-Ofelt analysis, which can lead to errors in estimates of derivative radiative quantities. In the recently published method, this Judd-Ofelt parameter can be accurately estimated from the excitation spectrum by [19]:

$$\Omega_6 = 0.459 \frac{n_6 n_1}{(n_6^2 + 2)^2} \frac{\bar{\lambda}_6}{\bar{\lambda}_1} \frac{\Gamma_6}{\Gamma_1} \cdot 10^{-20} \text{cm}^2. \tag{5}$$

where Γ are the integrated intensities of peaks in the excitation spectrum. Here 6 abbreviates $^7F_0 \rightarrow {}^5L_6$ and 1 in the subscript stands for $^7F_0 \rightarrow {}^5D_1$ transition.

From the Judd-Ofelt intensity parameters, the radiative transition probabilities for induced

electric dipole transitions can be calculated by [13]:

$$A_\lambda = \frac{64\pi^4}{3h} \frac{10^7}{\bar\lambda_\lambda^3} \frac{n_\lambda\left(n_\lambda^2 + 2\right)^2}{9} e^2 \Omega_\lambda U^\lambda \qquad (6)$$

and for magnetic dipole transition by:

$$A_1 = \frac{64\pi^4}{3h} \frac{10^7}{\bar\lambda_1^3} n_1^3 \cdot \qquad (7)$$

The total radiative transition probability, or the rate of spontaneous emission, is then equal to the inverse of the radiative lifetime:

$$A_R = \sum_{i=1,2,4,6} A_i = \frac{1}{\tau_R} \qquad (8)$$

Radiative transition probabilities provide estimates of emission branching ratios by:

$$\beta_{\lambda,1} = \frac{A_{\lambda,1}}{A_R} \qquad (9)$$

De-excitation rates, A_{obs}, are experimentally measured as the inverse of the observable emission lifetime, which then enables the calculation of the non-radiative rates:

$$A_{NR} = A_{obs} - A_R = \frac{1}{\tau_{obs}} - A_R \qquad (10)$$

Radiative transition probabilities enable the calculation of the emission cross-sections, given by the equation [20]:

$$\sigma_\lambda\left(\lambda_p\right) = \frac{\lambda_{max}^4}{8\pi c n_\lambda^2} \frac{\max I_\lambda}{I_\lambda} A_\lambda \qquad (11)$$

where c is the speed of light, and λ_{max} is the position of the peak maximum.

The Judd-Ofelt intensity parameters of SGF with various Eu^{3+} concentrations are given in Table 2, together with estimated derived quantities: transition probabilities, branching ratios, cross-sections, and lifetimes. All the quantities for transitions $^5D_0 \rightarrow {}^7F_{1,2,4}$ are estimated by JOES software [20], while quantities for $^5D_0 \rightarrow {}^7F_6$ emission are calculated by JOEX software [19]. Due to the lower emission intensity in the spectra, the analysis for the sample with 5% Eu^{3+} content has the largest error. Ω_2 parameter, as the measure of covalency and distortion of symmetry is largest for the samples with 60% and 80% of Eu^{3+}. A similar trend is observed with the Ω_4 parameter. Parameter Ω_6, associated with the rigidity of the matrix, decreases uniformly with an increase in Eu^{3+} concentration. The radiative transition probabilities confirm that the emission with the largest photon flux is to the $^7F_4$ level. Non-radiative component increases with Eu^{3+} doping concentration.

Table 1 Judd-Ofelt parameters for SrGdF:Eu^{3+}

| [Eu] (%)	5	10	40	60	80	100
$\Omega_2 \cdot 10^{20}$ (cm²)	0.41	0.99	0.98	1.17	1.17	1.08
$\Omega_4 \cdot 10^{20}$ (cm²)	3.08	4.19	4.63	4.78	4.79	4.30
$\Omega_6 \cdot 10^{20}$ (cm²)	1.91	1.38	1.10	0.88	0.86	0.85
A_1 (s⁻¹)	23.0	23.0	23.0	23.0	23.0	23.0
A_2 (s⁻¹)	6.3	14.2	14.0	16.8	16.9	15.5
A_4 (s⁻¹)	22.6	30.4	33.6	34.7	34.8	31.2
A_6 (s⁻¹)	1.1	0.8	0.6	0.5	0.5	0.5
β_1 (%)	44	34	32	31	31	33

β_2 (%)	12	21	20	22	22	22
β_4 (%)	43	44	47	46	46	44
β_6 (%)	2	1	1	1	1	1
$\sigma_1 \cdot 10^{22}$ (cm^2)	2.47	1.78	1.67	1.61	1.58	1.66
$\sigma_2 \cdot 10^{22}$ (cm^2)	0.74	0.74	0.74	0.84	0.84	0.79
$\sigma_4 \cdot 10^{22}$ (cm^2)	6.21	4.91	5.55	5.25	5.28	4.91
τ_{obs} (ms)	12.0	11.7	11.2	10.6	9.3	6.9
A_{obs} (s^{-1})	83.2	85.4	89.2	95.4	107.9	144.3
A_R (s^{-1})	52.9	68.3	71.3	75.0	75.1	70.1
A_{NR} (s^{-1})	30.3	17.1	17.9	20.4	32.7	74.1
τ_R (ms)	18.9	14.6	14.0	13.3	13.3	14.3

Mn^{5+}-doped $Ca_6Ba(PO_4)_4O$ powders

Synthesis: The conventional solid-state reaction was employed for the preparation of $Ca_6BaP_{4-4x}Mn_{4x}O_{17}$ ($x = 0.005, 0.0075, 0.0125, 0.01, 0.015, 0.02$) powder samples. Stoichiometric amounts of $CaCO_3$ (Alfa Aesar, 98%), $BaCO_3$ (Alfa Aesar, 99.8%), $(NH_4)H_2PO_4$ (Alfa Aesar, 98%), and MnO (Aldrich, 99.99%) were thoroughly mixed in an agate mortar for 1 h with an appropriate amount of ethanol. Mixtures of the raw materials were placed in alumina crucibles and heated in an air atmosphere at 600 °C for 6 h, ground in an agate mortar, and further calcinated at 1280 °C for 10 h.

Structural properties: The starting model used for Rietveld refinement and detailed structural analysis of the two key materials – the $Ca_6Ba(PO_4)_4O$ host and the sample containing 0.5%Mn – was the previously published crystal structure of $Ca_6Ba(PO_4)_4O$ determined from synchrotron powder diffraction data [21]. Refined parameters included the zero-point error, background polynomial terms, peak shape function terms, unit cell parameters, an isotropic atomic displacement parameter per atom type and atomic fractional coordinates, using bond valence sum restraints on the two P atoms. The key crystallographic parameters are summarized in Table 3. $Ca_6Ba(PO_4)_4O$ and $Ca_6Ba(PO_4)_4O$:0.5%Mn adopt monoclinic space group C2/m, with one Ba, two Ca, two P and seven O atoms in the asymmetric unit. Ba atoms are 12-coordinate, the two crystallographically unique Ca atoms are 7- and 8-coordinate, while both unique P atoms adopt tetrahedral coordination environments. Dopant Mn^{5+} ions replace P^{5+} on these two sites, which lie on a mirror plane (Wyckoff site 4 m in space group C2/m). In $Ca_6Ba(PO_4)_4O$, the average cation-oxygen bond lengths in the two tetrahedra are 1.534(13) and 1.529(15) Å, while bond angles range from 105.1(8) to 112.9(7)° and 105.3(7) to 112.8(9)°, with bond valence sums of 5.0(1) for both P atoms. In $Ca_6Ba(PO_4)_4O$:0.5%Mn, the coordination environments remain similar, as expected given a low doping level. Average bond lengths are 1.534(22) and 1.504(27) Å, while bond angles range from 103.4(16) to 112.8(12)° and from 105.5(13) to 112.5(11)°, with bond valence sums of 5.0(2) and 5.4(2) for P1 and P2 sites, (see Tables 4 and 5), respectively. The final Rietveld fits obtained are shown in Figure 5a-b, while the unit cell and the P atom environments are given in Figure 5c-d, respectively.
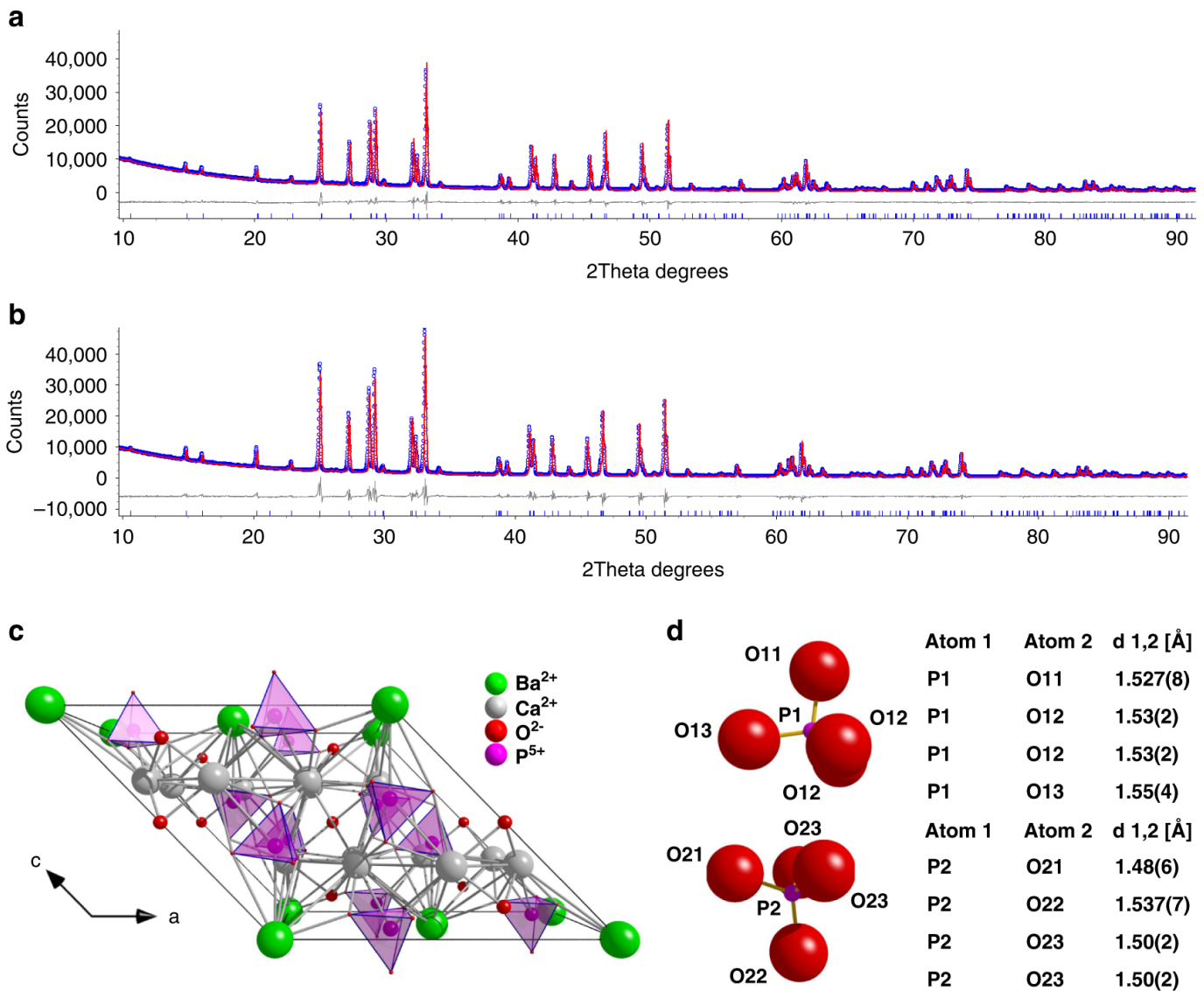
Figure 5 a) Rietveld fits for $Ca_6Ba(PO_4)_4O$, R_{wp} = 5.31%; b) Rietveld fit for $Ca_6Ba(PO_4)_4O:Mn^{5+}$, R_{wp} = 8.59%. In each case the blue curve represents the observed pattern, the red curve is the calculated pattern and the difference curves are shown in grey, while blue tick marks represent the positions of the Bragg peaks; c) The crystal structure of $Ca_6Ba(PO_4)_4O$, with the unit cell viewed along the b-axis; d) Geometries of two PO_4 tetrahedra with average P–O bond lengths in $Ca_6Ba(PO_4)_4O:Mn^{5+}$

Table 3. Summary of structural data for $Ca_6Ba(PO_4)_4O$ and $Ca_6Ba(PO_4)_4O:Mn^{5+}$ (space group C2/m).

	Exp. $Ca_6Ba(PO_4)_4O$			**Exp. $Ca_6Ba(PO_4)_4O:Mn$**		
a, Å	12.3006(1)			12.2973(2)		
b, Å	7.10472(7)			7.10258(1)		
c, Å	11.71540(9)			11.7125(1)		
β, º	134.4619(4)			134.4552(8)		
V, Å³	730.73(1)			730.22(2)		
Fractional atomic coordinates						
	x	y	z	x	y	z
Ba	0	0	0	0	0	0
Ca1	0.7196(6)	0	0.3117(8)	0.719(1)	0	0.311(1)
Ca2	0.0505(4)	0.7665(5)	0.6929(4)	0.0505(8)	0.766(1)	0.6930(7)
O	0	0	0.5	0	0	0.5

O11	0.399(1)	0	0.5822(5)	0.394(2)	0	0.5822(8)
O12	0.281(1)	-0.175(1)	0.3367(6)	0.281(2)	-0.175(2)	0.336(1)
O13	0.120(1)	0	0.366(1)	0.120(2)	0	0.365(2)
O21	0.289(1)	0	0.106(2)	0.290(3)	0	0.104(3)
O22	0.242(1)	0	-0.1373(5)	0.241(3)	0	-0.1368(7)
O23	0.462(1)	-0.179(1)	0.114(1)	0.461(2)	-0.174(2)	0.114(1)
P1	0.2673(6)	0	0.3999(2)	0.266(1)	0	0.3998(2)
P2	0.3659(8)	0	0.0469(2)	0.365(1)	0	0.0469(3)
Calculated						
	GGA			**LDA**		
a, Å	12.4130			12.0755		
b, Å	7.1493			6.9658		
c, Å	11.8311			11.4881		
β, º	134.3735			134.4363		
V, Å^3	750.489			689.983		
Fractional atomic coordinates						
	x	y	z	x	y	z
Ba	x	y	z	x	y	z
Ca1	0	0	0	0	0	0
Ca2	0.71621	0	0.30969	0.71770	0	0.31126
O	0.05261	0.76649	0.69427	0.05232	0.76734	0.69366
O11	0	0	0.5	0	0	0.5
O12	0.39056	0	0.58173	0.39300	0	0.58450
O13	0.28457	-0.17593	0.34032	0.28484	-0.17824	0.33934
O21	0.11338	0	0.34744	0.11195	0	0.34779
O22	0.29114	0	0.11117	0.29072	0	0.11278
O23	0.24386	0	-0.13571	0.24374	0	-0.13726
P1	0.46648	-0.17433	0.11348	0.46930	-0.17679	0.11594
P2	0.26593	0	0.39888	0.26621	0	0.39890

Table 4. P – O bond lengths [Å].

	Undoped Ca$_6$Ba(PO$_4$)$_4$O		Mn^{5+} doped Ca$_6$Ba(PO$_4$)$_4$O	
	P1	**P2**	**P1**	**P2**
	1.530(5)	1.52(3)	1.527(8)	1.48(6)
	1.523(13)	1.542(5)	1.53(2)	1.537(7)
	1.523(13)	1.527(12)	1.53(2)	1.50(2)
	1.56(2)	1.527(12)	1.55(4)	1.50(2)
Avg:	**1.534(13)**	**1.529(15)**	**1.534(22)**	**1.504(27)**

Table 5. O – P – O angles and their difference, δ, to regular tetrahedron angle of 109.5º.

Undoped Ca$_6$Ba(PO$_4$)$_4$O				Mn^{5+} doped Ca$_6$Ba(PO$_4$)$_4$O			
P1	**δ [º]**	**P2**	**δ [º]**	**Mn1**	**δ [º]**	**Mn2**	**δ [º]**
109.8(12)	0.3	112.8(9)	3.3	110(2)	0.5	111.9(17)	2.4
107.9(4)	-1.6	105.3(7)	-4.2	108.8(8)	-0.7	105.5(13)	-4.0
107.9(4)	-1.6	105.3(7)	-4.2	108.8(8)	-0.7	105.5(13)	-4.0
105.1(8)	-4.4	109.1(11)	-0.4	103.4(16)	-6.1	109(2)	-0.5
112.9(7)	3.4	111.9(6)	2.4	112.8(12)	3.3	112.5(11)	3.0
112.9(7)	3.4	111.9(6)	2.4	112.8(12)	3.3	112.5(11)	3.0
Avg (δ)	*-0.08*		*-0.12*	Avg (δ)	*-0.07*		*-0.42*
Avg (abs(δ))	2.4		2.8	Avg (abs(δ))	2.4		2.8

Photoluminescent properties: Figures 6 a) and b) display the absorption, color (inset in Figure 6a), and emission spectra of $Ca_6Ba(PO_4)_4O$: 0.5%Mn^{5+} powder.
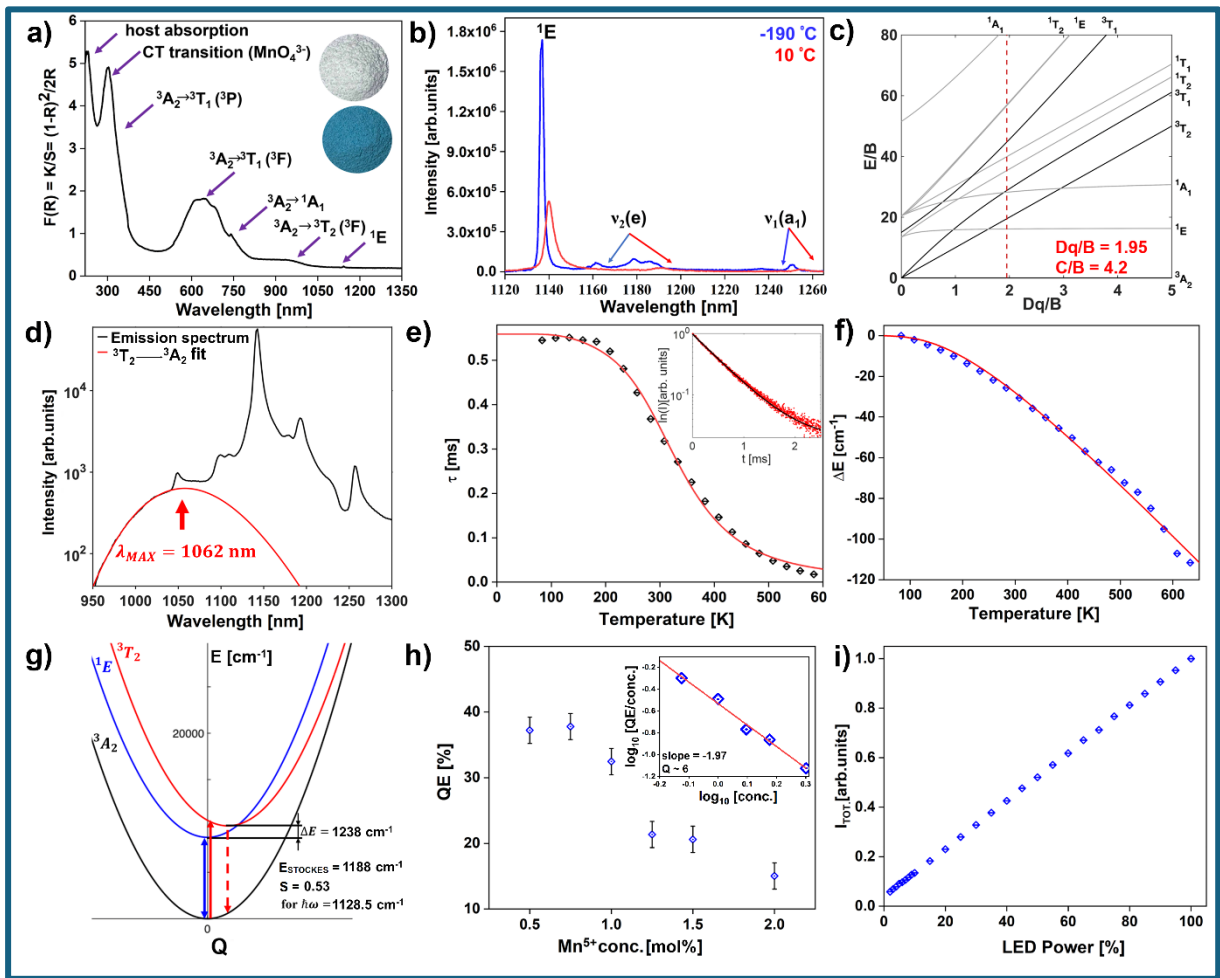
Figure 6. Optical properties of the $Ca_6Ba(PO_4)_4O$:Mn^{5+} powder: a) The Kubelka-Munk transformation of the $Ca_6Ba(PO_4)_4O$:Mn^{5+} diffuse reflectance; inset shows photographs of the $Ca_6Ba(PO_4)_4O$ (white) and $Ca_6Ba(PO_4)_4O$:Mn^{5+} (blue) powders, b) Emission spectra measured at -190°C and 10°C, c) Tanabe-Sugano diagram for $3d^2$ electron configuration in tetrahedral coordination, d) Emission spectrum of the $Ca_6Ba(PO_4)_4O$:Mn^{5+} measured at room temperature (black line) and the fit to the Gaussian of the $^3T_2 \rightarrow {}^3A_2$ emission peak (red line) showing its maximum 1062 nm / 9416 cm^{-1}; spectra shown in logarithm scale, e) temperature dependence of the excited state lifetime (symbols – experimental data, solid line – the fit to Eq. (4)); inset: emission decay measured at 208 K, f) Temperature dependence of the ^1E emission peak spectral position (symbols – experimental data, solid line – the fit to Eq. (5)), g) The estimate of configurational diagram based on the spectroscopic data with calculated Stokes shift ($E_{Stockes}$) and Huang-Rhys parameter (S), h) Photoluminescence internal quantum efficiency (QE) of $Ca_6Ba(PO_4)_4O$:Mn^{5+} powders for different concentrations of Mn; inset shows linear dependence of the log_{10}(QE/concentration) vs log_{10}(concentration) for data equal and above critical concentration (0.75%) with a slope of -1.97 indicating that a multipolar dipole-dipole mechanism is responsible for the concentration quenching of emission, and i) The linear dependence of $Ca_6Ba(PO_4)_4O$:Mn^{5+} emission intensity on excitation power.

Figure 6a) depicts the Kubelka-Munk transformation of the $Ca_6Ba(PO_4)_4O$:Mn^{5+} powder diffuse reflection measured between 220 and 1350 nm. The $O^{2-} \rightarrow Mn^{5+}$ charge-transfer band appears at around 301 nm (33222 cm^{-1}) as expected for the tetraoxo-coordinated Mn^{5+} [22] and the peak at the lower wavelength (225 nm) is associated with the intrinsic host absorption. The strong absorption around 639 nm (15649.5 cm^{-1}) is associated with the $^3A_2 \rightarrow {}^3T_1(^3F)$ electronic transition, which is electric dipole-allowed in an undistorted tetrahedral symmetry and is composed of three

overlapping components due to the removal of the orbital degeneracy of the $^3T_1(^3F)$ state with the site symmetry lowering from T_d to C_s. The weak shoulder at about 943 nm (10604.5 cm^{-1}) corresponds to the symmetry forbidden $^3A_2 \rightarrow {}^3T_2(^3F)$ transition (in T_d site symmetry) and becomes partially allowed with a symmetry lowering. The electric dipole-allowed $^3A_2 \rightarrow {}^3T_1(^3P)$ transition that corresponds to a two-electron jump is located at approximately 369 nm (27100 cm^{-1}) and is barely visible due to the much more intense charge transfer band. The spin-forbidden transitions to the singlet states $^1A_1(^1G)$ at 740 nm (13513.5 cm^{-1}) and $^1E(^1D)$ at 1140 nm (8772 cm^{-1}) are weak, sharp, and only weakly depend on the host materials properties. The transitions to $^1T_{1,2}$ singlet states are difficult to observe in the spectrum since they are very weak and superimposed on the main and stronger bands.

Emission spectra of Ca$_6$Ba(PO$_4$)$_4$O:Mn^{5+} powder measured at -190°C and 10°C are shown in Figure 6b) with blue and red lines, respectively, and are typical for emissions from transitions of 3d^2 electronic configuration in a tetrahedral environment as described by the Tanabe-Sugano diagram, Figure 6c). The spectra show ultranarrow emission bands (FWHM = 3 nm (20 cm^{-1}) at -190°C; FWHM = 5 nm (35 cm^{-1}) at 10°C) from the $^1E \rightarrow {}^3A_2$ intraconfigurational transition (1140 nm), followed by vibrational sidebands with progressions of $\approx$ 320 cm^{-1} (($\nu_2(e)$) and $\approx$ 800 cm^{-1} (($\nu_1(a_1)$). This indicates the coupling of the ^1E excited state and the non-totally symmetric $\nu_2(e)$ mode of MnO$_4^{3-}$, i.e., a dynamic Jahn-Teller effect.

The very small splitting of ^1E emission band is due to only weakly distorted MnO$_4$ tetrahedra (see Table 3) and it is barely visible with our instrument resolution at the emission spectrum measured at low temperatures (-190°C). The low-intensity broad emission band from the $^3T_2(^3F) \rightarrow {}^3A_2$ transition is centered at 1062 nm (9416 cm^{-1}) and can be resolved only spectral deconvolution, Figure 6d).

Temperature dependence of the ^1E lifetime and emission peak spectral position are shown in Figures 6e) and f), respectively. The ^1E level emission decays show lifetime values of about 350 μs at room temperature and 560 μs at low temperatures. The temperature dependence of lifetime, Figure 6e), shows that a low-temperature lifetime value is approximately the value of a radiative lifetime. Considering that the excited state is separated in energy from the ground state by 8772 cm^{-1}, almost eight quanta of the highest vibrational frequencies of the phosphor ($\approx$ 1100 cm^{-1}) is needed to bridge the gap. Thus, a multiphonon non-radiative relaxation is not probable as the emission quenching mechanism. The ^1E emission deactivation through the crossing with a charge transfer band is also not probable due to very high energy difference. Therefore, we assume that the thermal quenching of the ^1E state population takes place by a thermally activated cross-over via $^3T_2$ state, see Figure 6g), similarly to Mn^{4+} activated phosphors. The temperature dependence of the emission lifetime, shown in Figure 4e), can be described by the following equation:

$$\tau(T) = \frac{\tau_{R0} \cdot \tanh(h\nu/2k_BT)}{1 + (\tau_{R0} \cdot \tanh(h\nu/2k_BT)/\tau_{NR}) \cdot \exp(-\Delta E/k_BT)}, \qquad (12)$$

where τ_{R0} = 560 ± 19 μs is the radiative lifetime at T = 0 K, k_B=0.69503476 cm^{-1}/K is the Boltzmann constant, $h\nu$ = 448 ± 90 cm^{-1} is the average energy of phonon coupled to the $^1E \rightarrow {}^3A_2$ transition, $1/\tau_{NR}$ = 1527 ± 120 ms^{-1} is the nonradiative decay rate, ΔE = 1631 ± 200 cm^{-1} is the activation energy of the process (the cross-over via the $^3T_2$ state), and T represents the temperature. The smaller the configuration coordinate parabola offset between the ground state ($^3A_2$) and the $^3T_2$ state, the larger the cross-over energy ΔE (activation energy of the process) needed to activate the non-radiative de-

excitation process. Thus, the $^1E \rightarrow {}^3A_2$ emission of Mn^{5+} activated phosphors, which have large $^3T_2$ energies and smaller Stokes shifts, will start to quench at higher temperatures.

The shift of ^1E emission band with energy is shown in Figure 6(f). It can be described by the following equation [23, 24]:

$$\delta E \text{ [cm}^{-1}] = \alpha \cdot \left(\frac{T}{\theta_D}\right)^4 \cdot \int_0^{T/\theta_D} \frac{x^3}{e^x - 1} dx, \tag{13}$$

where θ_D = 783 ± 12 K is the Debye temperature of the host material, $x = \hbar\omega_D/k_B T = \theta_D/T$, ω_D is Debye cut-off frequency, and α = -650 ± 17 cm^{-1} represents the electron-phonon coupling coefficient. The relatively high Debye temperature indicates a rigid structure which favors efficient emissions from optical centers [25].

The concentration dependence of an internal quantum efficiency (QE) is given in Figure 6h). The largest value of 37.5 ± 2.0 % is recorded for the 0.5% Mn^{5+} doped sample, after which the concentration quenching of emission occurs. This is a relatively high value for an NIR-emitting phosphor, and comparable to one obtained in $Ba_3(PO4)_2$ [26]. The $\log_{10}$(QE/concentration) vs $\log_{10}$(concentration) plot has a -1.97 slope, which is close to -2, which undoubtedly indicates that a multipolar electric dipole-dipole mechanism is responsible for the concentration quenching of emission. The linear dependence of $Ca_6Ba(PO_4)_4O:Mn^{5+}$ emission intensity on excitation power, Figure 6i), is expected for the typical downshifting photoluminescence emission process.

The $3d^2$ electronic configuration of Mn^{5+} in a tetrahedral environment is described by the Tanabe-Sugano model for $3d^8$ electronic configuration in octahedral symmetry [27], see Figure 6c). The crystal field and Racah parameters are calculated from the following equations using data from diffuse reflection and emission spectra [28, 29]:

$$Dq = \frac{E\left({}^3A_2 \rightarrow {}^3T_2\right)}{10} = \frac{10604.5}{10} \text{ cm}^{-1} = 1060 \text{ cm}^{-1} \tag{14}$$

$$x = \frac{E\left({}^3A_2 \rightarrow {}^3T_1\right) - E\left({}^3A_2 \rightarrow {}^3T_2\right)}{Dq} = \frac{15649.5 - 10604.5}{1060.45} = 4.757 \tag{15}$$

$$B = \frac{x^2 - 10x}{15 \cdot (x - 8)} \cdot Dq = 544 \text{ cm}^{-1} \quad \rightarrow \quad \frac{10Dq}{B} = 19.5 \tag{16}$$

$$C = \frac{1}{2} \cdot \left(E\left({}^3A_2 \rightarrow {}^1E\right) - 10Dq - 8.5B + \frac{1}{2}\sqrt{400Dq^2 + 40DqB + 49B^2}\right) = 2292 \text{ cm}^{-1} \tag{17}$$

$$\frac{C}{B} = 4.21 \tag{18}$$

By comparing the obtained Dq, B and C parameters with literature data, Table 6, one can observe that $Ca_6Ba(PO_4)_4O$ provides the smallest Dq and the largest B parameters amongst all phosphate hosts, and that Li_3VO_4 is the only host with a smaller Dq (considering available data).

Table 6. Comparison of the *Dq*, *B* and *C* parameters (all in cm^{-1}) for the tetrahedrally coordinated Mn^{5+} ions in different crystalline solids

Host material	*Dq*	*B*	*C*	Reference
Li$_3$PO$_4$	1208	475	2556	[42]
Ca$_2$PO$_4$Cl	1162	455	2657	[42]
Y$_2$SiO$_5$	1133	550	2255	[43]
Sr$_5$(PO$_4$)$_3$Cl	1100	500	2320	[3]
YAlO$_3$	1100	485	2256	[44]
Sr$_{10}$(VO$_4$)$_6$F$_2$	1088	518	2321	[45]
Ca$_6$Ba(PO$_4$)$_4$O	1060	544	2292	*This work*
Li$_3$VO$_4$	1049	646	2006	[46]

By considering the obtained parameters and the configuration coordinate diagram, Figure 6g), the relatively small value of Huang-Rhys parameter S=0.53 is found for the assumed coupling to the ν_{1+} ν_L/ ν_{3+} ν_L vibrational mode with energy $\hbar\omega = 1128.5$ cm^{-1}.

The Slater parameters are calculated from Racah parameters by the simple relations [30, 31]:

$$F^{(2)} = 49F_2 = 7(7B + C) = 42271 \text{ cm}^{-1}, \tag{19}$$

$$F^{(4)} = 441F_4 = 441\frac{C}{35} = 28877 \text{ cm}^{-1}. \tag{20}$$

Both values are considerably reduced from the free-ion values of $F^{(2)} = 91427$ cm^{-1} and $F^{(4)} = 56625$ cm^{-1}.

As follows from the Tanabe-Sugano diagram for the 3d^2 configuration in the tetrahedral crystal field (Figure 6c)), the energy separation between the ground state ^{3}A$_2$ and the first excited state ^{1}E (in the strong crystal field) is practically independent on the crystal field strength (both states are parallel to each other). At the same time, this energy interval is very close to the energy interval between the ^{3}F and ^{1}D states of the free ion, which is determined by the Racah parameters B and C, which vary from host to host because of the covalent effects. As a result, the nephelauxetic effect is dominating in this case.

We have tested the performance of Mn^{5+} activated Ca$_6$Ba(PO$_4$)$_4$O (the sample containing 0.75% Mn since it showed the best quantum efficiency) as a NIR luminescent thermometer operating in the second biological window and in the physiological temperature range. As can be seen from Fig 7a), when temperature increases, the broad emission peak from the ^{3}T$_2$ level in the 950 nm to 1030 nm range also increases in intensity, while the intensity of narrow emission peak from the ^{1}E level around 1150 nm decreases with temperature. This occurs due to thermalization between ^{1}E and ^{3}T$_2$ levels where the energy difference between these two levels (ΔE_T) is bridged by thermally exited electrons. Consequently, a simple Boltzmann-type relation for luminescence intensity ratio (LIR) between the two abovementioned emission intensities applies [32, 33]:

$$LIR(T) = \frac{I(\,^3T_2)}{I(\,^1E)} = B \cdot \exp\left(-\frac{\Delta E_T}{k_B T}\right), \tag{21}$$

where B is a temperature-invariant constant and T represent temperature. The fit of Eq. (13) (full line, Fig. 7b) to experimental LIR data (diamond markers, Fig. 7b)) is almost perfect ($R^2 = 0.997$) and provides ΔE_T of 1216 cm^{-1} which agrees with the energy difference obtained from spectroscopy (Figure 6g)). To experimentally determine the uncertainty in the LIR (error budget), 50 emission spectra were acquired at each temperature. Then, the measurement distribution mean was used as the LIR value while a standard deviation (σ_{LIR}) was used as an uncertainty in LIR (as shown in the insert of Fig. 7b) on the LIR value distribution measured at 30 °C.
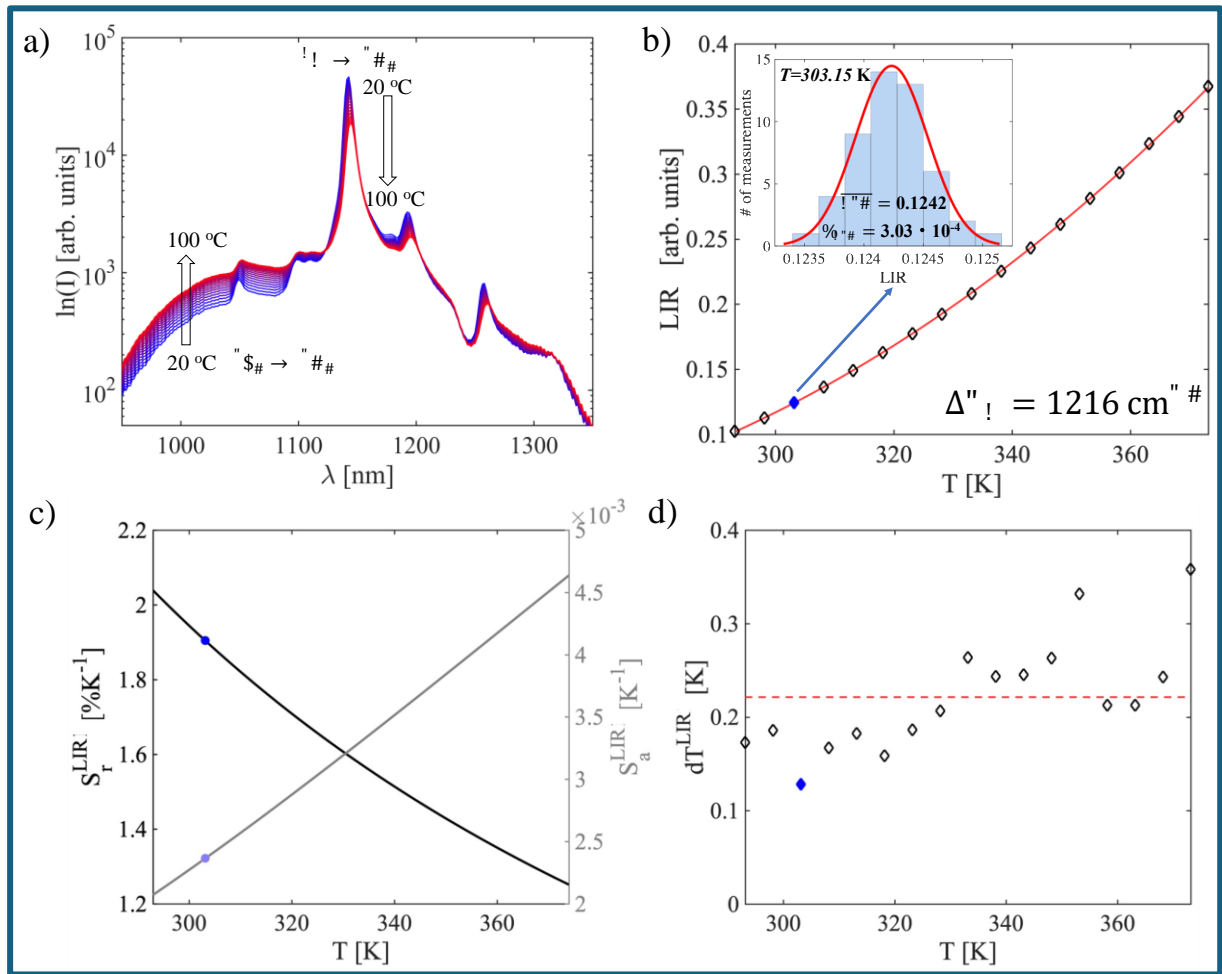
Figure 7. a) Photoluminescence emission spectra of $Ca_6Ba(PO_4)_4O:Mn^{5+}$ powder measured at different temperatures; b) LIR as a function of temperature (experimental data - diamond markers; fit to Eq. (13) - full line); insert: the LIR distribution histogram measured at 303.15 K (30 °C) – filled diamond marker; c) Calculated absolute and relative sensitivities (marked values at 303.15 K (30 °C)); d) Experimentally obtained values for temperature resolution – filled diamond marker represents the value at 303.15 K (30 °C).

The absolute (S_a) and relative (S_r) sensitivities of the thermometer were then calculated from the following equations:

$$S_a[K^{-1}] = \left|\frac{\partial LIR}{\partial T}\right|, \quad S_r[\%K^{-1}] = 100\% \cdot \left|\frac{\partial LIR}{\partial T}\frac{1}{LIR}\right|, \tag{22}$$

and presented in Fig 7c (blue dots represent values obtained at a temperature of 30 °C). The relative sensitivity value varies from 2.35%K^{-1} to 1.26%K^{-1} over the measurement range, being 1.92%K^{-1} at 30°C. These are relatively high values [34], especially for luminescence thermometers operating in the second biological transparency window (> 1000 nm). For example, Gschwend et al [35] obtained a relative sensitivity of 0.43%K^{-1} for an LIR thermometer based on Mn^{5+}-activated Ba$_3$(PO$_4$)$_2$, and Shen et al [36] obtained a relative sensitivity of 1.3%K^{-1} for an LIR thermometer based on Ag$_2$S quantum dots.

The temperature resolution (uncertainty in measured temperature, δT) is determined as a ratio between experimentally obtained LIR uncertainty (σ_{LIR}) and absolute sensitivity (S_a) for a given temperature, Fig. 7d:

$$\delta T = \frac{\sigma_{LIR}(T)}{S_a(T)}, \tag{23}$$

and it has an average value of 0.21 K. Finally, repeatability of measurement (R) is quantified as:

$$R = 1 - \frac{max|\overline{LIR} - LIR_i|}{\overline{LIR}}, \tag{24}$$

where $\overline{LIR}$ is the average LIR measured at a certain temperature over all LIR_i acquired. Based on experimental data, an R value of 0.97 (97 %) is obtained.

Er^{3+} and Er^{3+}/Yb^{3+} doped LaPO$_4$ colloidal nanoparticles

Synthesis: Two colloidal LaPO$_4$:5 mol%Er^{3+} and LaPO$_4$:2 mol% Er^{3+}, 20 mol% Yb^{3+} samples were synthesized using the solution of trisodium citrate dihydrate added drop by drop to the mixture of La(NO$_3$)$_3$ × 6H$_2$O and rare-earths nitrates (Er (NO$_3$)$_3$ × 6H$_2$O, Yb(NO$_3$)$_3$ × 6H$_2$O) in the stoichiometric ratio at room temperature. The white precipitate consisting of the La^{3+}-(Er^{3+}/Er^{3+},Yb^{3+})-Cit$_3$ complex is formed, then completely dissolved by vigorous stirring and adding (NH$_4$)$_2$HPO$_4$ water solution. Further, the resulting transparent solution was stirred for 1 h at room temperature at pH 5.5. The dialysis against distilled water for 24 h removed excess ions (pH = 7). Powder samples used for XRD analysis were obtained by evaporation of aqueous colloidal solutions. The amounts of precursors used for synthesizing samples are given in Table 7.

**Table 7.** The amounts of precursors needed for synthesizing samples.

Sample	m (La(NO$_3$)$_3$×6H$_2$O)	m (Na$_3$-citrate × 2H$_2$O)	m (Er(NO$_3$)$_3$ × 6H$_2$O)	m (Yb(NO$_3$)$_3$ × 5H$_2$O)	m ((NH$_4$)$_2$HPO$_4$)
LaPO$_4$	0.2195 g	0.1838 g	/	/	0.0330 g
LaPO$_4$:5 mol%Er^{3+}	0.2086 g	0.1838 g	0.0116 g	/	0.0330 g
LaPO$_4$:2 mol% Er^{3+}, 20 mol% Yb^{3+}	0.1712 g	0.1838 g	0.0046 g	0.0449 g	0.0330 g

Structural and morphological properties: Figure 8 (left) shows X-ray diffractograms of representative LaPO4:5 mol%Er^{3+} powder sample obtained by evaporation of aqueous colloidal solutions presented together with ICDD Card No. 01-084-0600 for monoclinic LaPO4. Observed wide diffractions indicate ultra-small particle size confirmed with transmission electron microscopy presented as Figure 8 (right). TEM images show ultra-small particles with around 2 nm size.
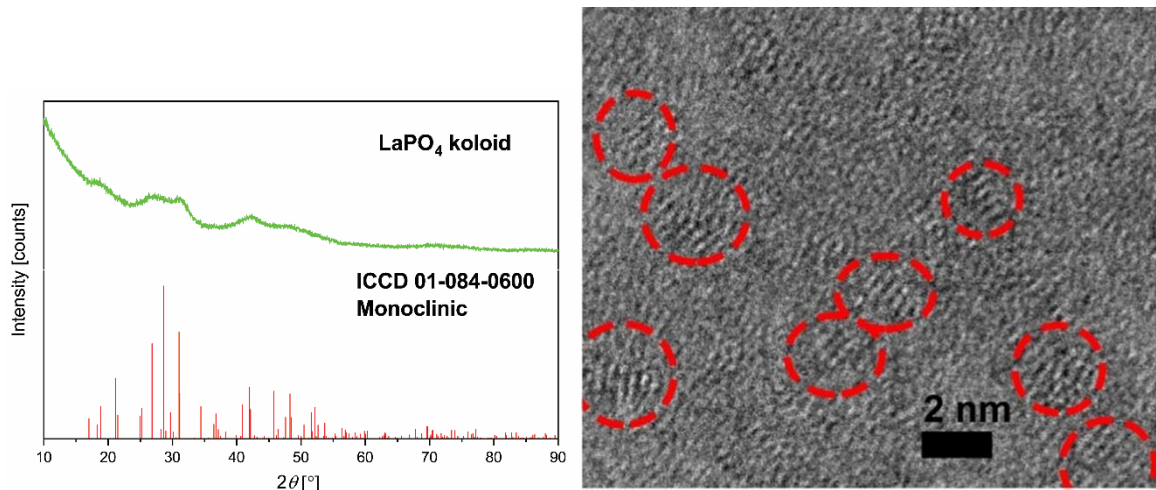
Figure 8 (left) X-ray diffractogram of representative LaPO$_4$:5 mol%Er^{3+} powder sample obtained by evaporation of aqueous colloidal solutions presented together with ICDD Card No. 01-084-0600 for monoclinic LaPO4 and (right) transmission electron microscopy image of the sample.

Photoluminescent properties: Figure 9 presents photoluminescent excitation and emission spectra of LaPO$_4$:5 mol%Er^{3+} (Figure 9a-b) and LaPO$_4$:2 mol% Er^{3+}, 20 mol% Yb^{3+} samples (Figure 9c-d). Spectra shows blue/green emission originating from Er^{3+} transitions while broad structure of the spectra is a consequence of ultra-small size of the colloid particles.
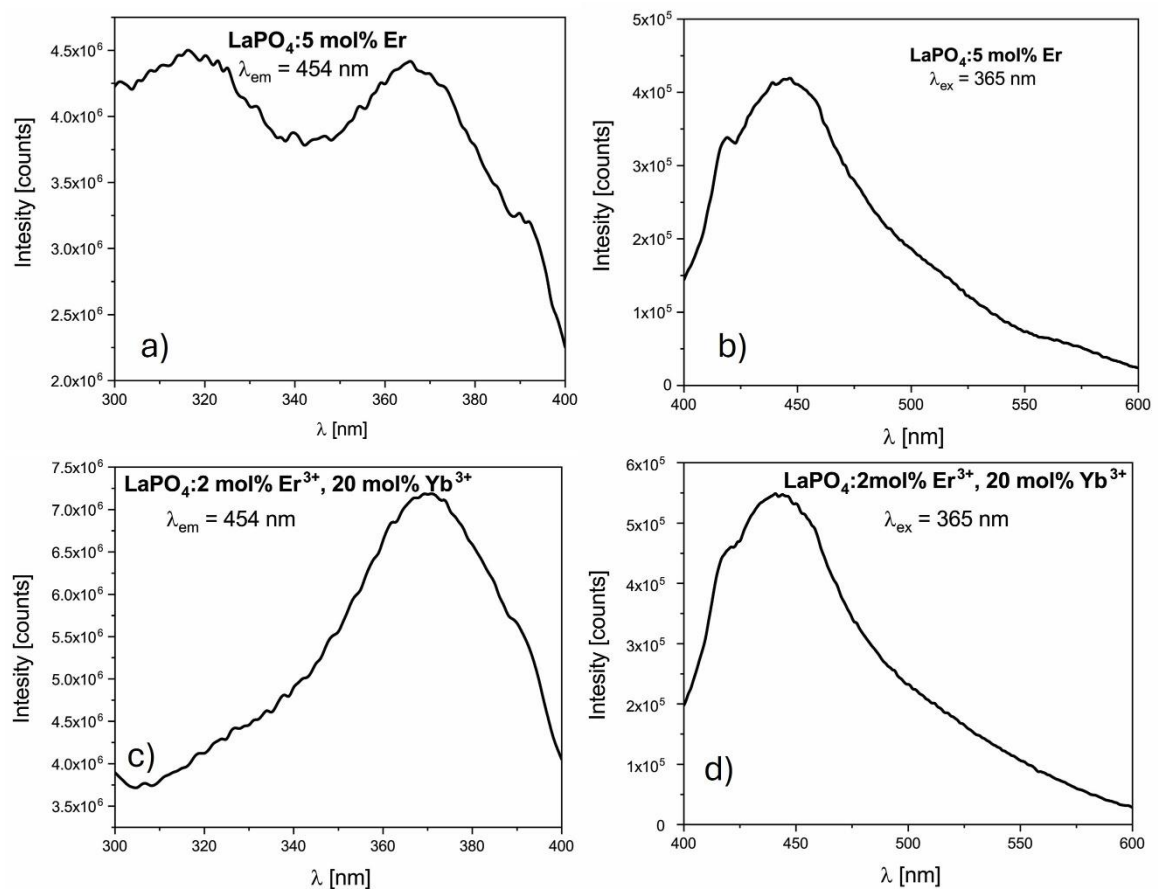
Figure 9 Photoluminescent excitation and emission spectra of (a-b) LaPO$_4$:5 mol%Er^{3+} and (c-d) LaPO$_4$:2 mol% Er^{3+}, 20 mol% Yb^{3+} samples.

Er³⁺, Nd³⁺ and Tm³⁺-doped YVO₄ colloidal nanoparticles

Synthesis: Three colloidal samples: Er³⁺, Nd³⁺ and Tm³⁺-doped YVO₄ were synthesized in accordance with the method described earlier [37-39]. The concentration of each precursor solution in water was 0.05 M. An aqueous solution of trisodium citrate (15 mL) was added drop-wise to the mixture (total volume was 20 mL) of $Er(NO_3)_3 \times 6H_2O$, $Nd(NO_3)_3 \times 6H_2O$ and $Tm(NO_3)_3 \times 6H_2O$ in stoichiometric ratios (25 mol% of Er³⁺, 25 mol% of Nd³⁺ and 25 mol% of Tm³⁺ ions to Y³⁺ ions) at room temperature. After vigorous stirring and slow addition of NH_4VO_3 dissolved in 0.15 M NaOH (15 mL), the white precipitate of the RE³⁺-citrate complex was completely dissolved, and the corresponding vanadete-based nanostructures slowly grown. Then, as-prepared colloidal solutions were additionaly stirred and heated at 60 ºC for 1 h, and finally dialysed against water for 24 h. The obtained colloidal NPs (concentration of NPs ~ 6 mg/mL) were used for luminescent properties studies. Powder samples used for XRD analysis were obtained by evaporation of aqueous colloidal solutions.

Structural and morphological properties: XRD pattern of representative Er³⁺-activated YVO₄ ultrasmall NPs, together with standard data for single tetragonal zircon-type phase (ICDD card No 01-086-0996) with the space group of I41/amd is shown in Figure 10.
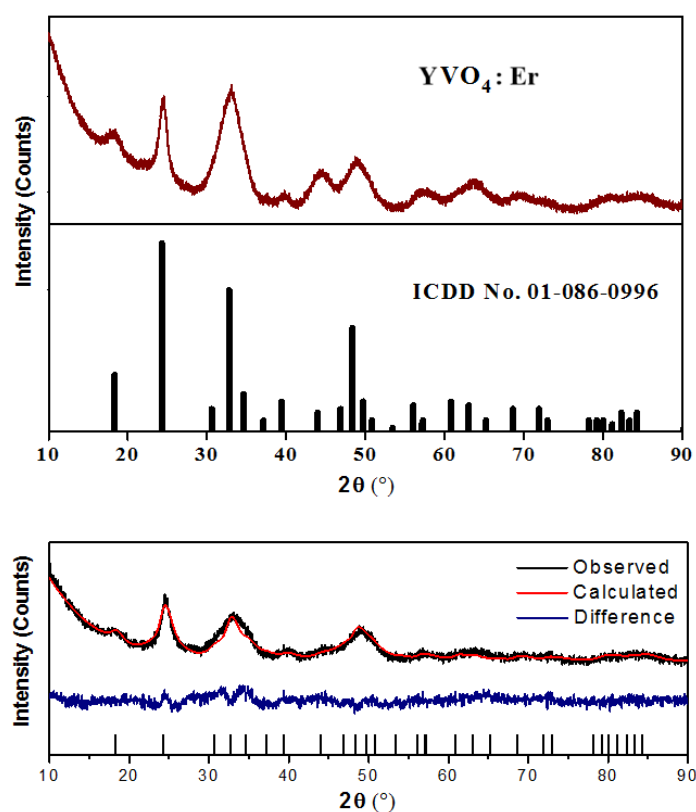

Figure 10 XRD pattern of representative Er³⁺-activated YVO₄ ultrasmall NPs, together with standard data for single tetragonal zircon-type phase (ICDD card No 01-086-0996).

All synthesized NPs have the same morphology and representative TEM image of the Er³⁺-activated YVO₄ nanoparticles is shown in Figure 11a. Figures show ultra-small crystallites of approximately 2.4 nm in diameter (when measured from edge to edge) and a narrow size distribution (standard deviation, σ_d = 0.5 nm). The mean particle size roughly equals the crystallite size calculated using XRD, which suggests that each particle consists of a single crystallite.
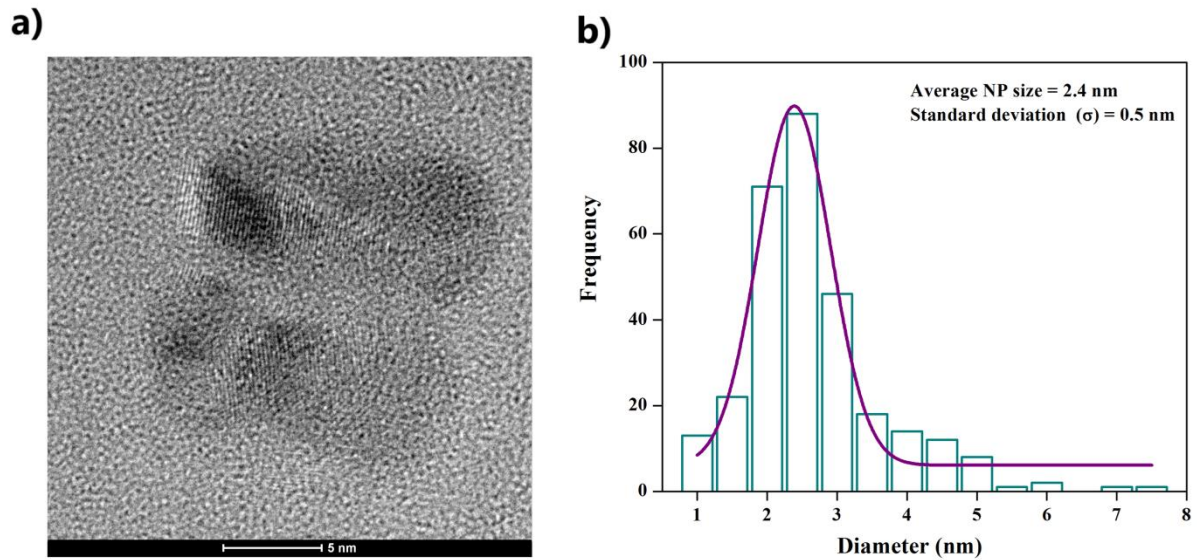
**Figure 12** a) TEM images and b) the particle-size distribution histograms representative $YVO_4:Er^{3+}$ nanoparticles.

UV-VIS optical and photoluminescent properties: UV-VIS absorption spectrum of representative $YVO_4:Er^{3+}$ colloid sample is presented in Figure 13. The absorption bands correspond to Er^{3+} absorptions from the $^4I_{15/2}$ level to different excited levels: $^4G_{11/2}$ (~ 377 nm), $^4F_{7/2}$ (~ 487 nm), $^4S_{3/2}$ (~ 525 nm) and $^4F_{9/2}$ (~ 655 nm).
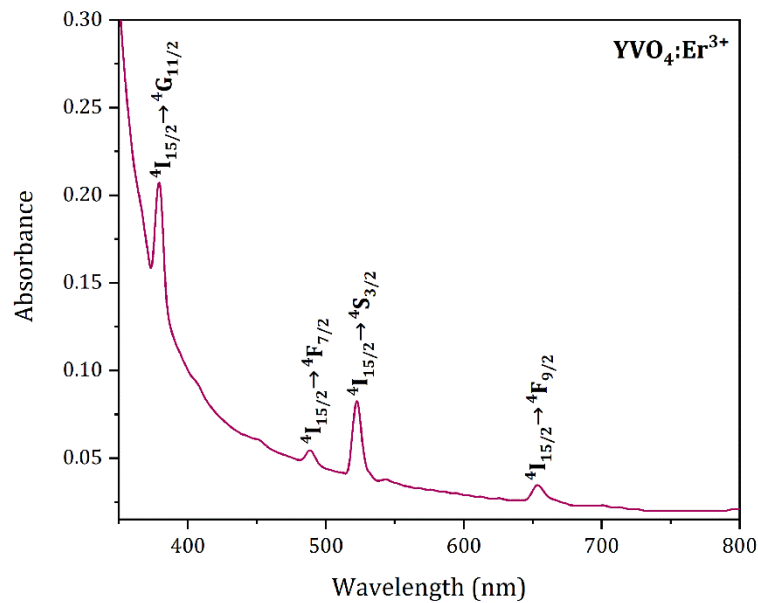
Figure 13 UV-VIS absorption spectra of representative $YVO_4:Er^{3+}$ colloid sample.

Photoluminescent excitation and emission spectra are presented for $YVO_4:Tm^{3+}$ colloid sample in Figure 14. Emission spectra show wide emission peaks that correspond to $^1D_2 \rightarrow {}^3F_4$ (~ 465 nm) and $^3P_0 \rightarrow {}^3F_{2,3}$ and $^1G_4 \rightarrow {}^3H_6$ transitions (wide band peaking at ~ 540 nm). Again, broad structure of the spectra is a consequence of ultra-small size of the colloid particles.
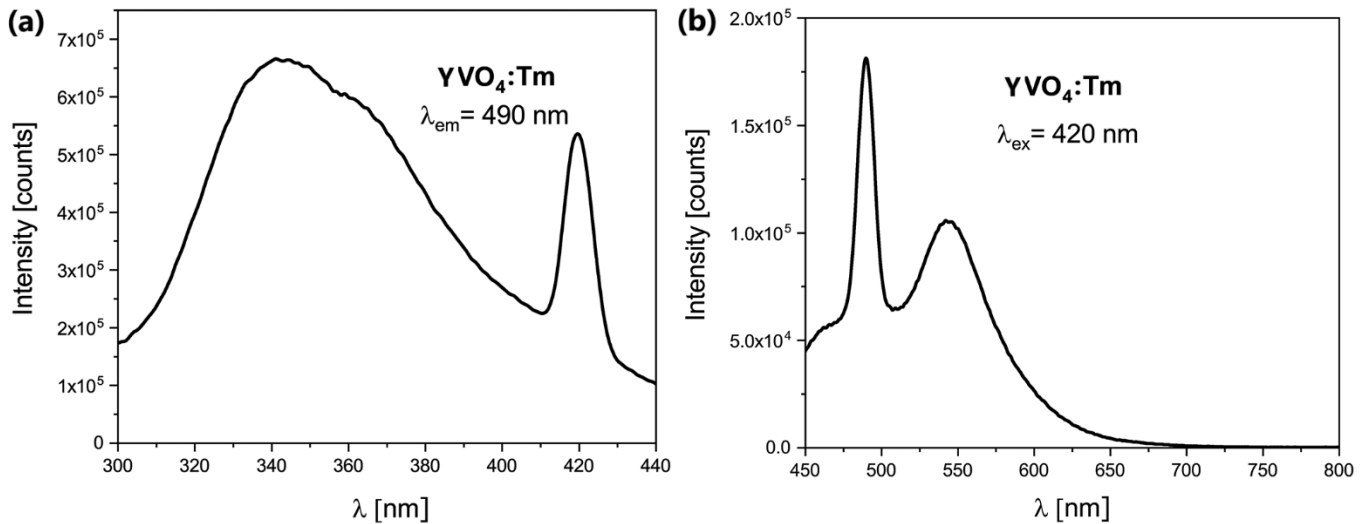
Figure 14 Photoluminescent excitation and emission spectra for $YVO_4:Tm^{3+}$ colloid sample.

References:

1. B. Milićević, J. Periša, Z. Ristić, K. Milenković, Ž. Antić, K. Smits, M. Kemere, K. Vitols, A. Sarakovski, M. Dramićanin, Hydrothermal synthesis and properties of Yb^{3+}/Tm^{3+} doped Sr_2LaF_7 upconversion nanoparticles, Nanomaterials, 13 (2022), p. 30, 10.3390/nano13010030
2. R.D. Shannon, Revised effective ionic radii and systematic studies of interatomic distances in halides and chalcogenides, Acta Crystallogr. Sect. A, 32 (1976), pp. 751-767, 10.1107/S0567739476001551
3. P. Dang, G. Li, X. Yun, Q. Zhang, D. Liu, H. Lian, M. Shang, J. Lin, Thermally stable and highly efficient red-emitting Eu^{3+}-doped $Cs_3GdGe_3O_9$ phosphors for WLEDs: non-concentration quenching and negative thermal expansion, Light Sci. Appl., 10 (2021), p. 29, 10.1038/s41377-021-00469-x
4. M. Dejneka, E. Snitzer, R.E. Riman, Blue, green and red fluorescence and energy transfer of Eu^{3+} in fluoride glasses, J. Lumin., 65 (1995), pp. 227-245, 10.1016/0022-2313(95)00073-9
5. L. Xiang, X. Zhou, L. Li, F. Ling, Y. Li, J. Li, H. Yang, Comparative study on the anomalous intense $^5D_0 \rightarrow {}^7F_4$ emission in Eu^{3+} doped Sr_2MNbO_6 (M=Ga, In, Gd) phosphors, J. Lumin., 267 (2024), Article 120370, 10.1016/j.jlumin.2023.120370
6. G. Blasse, Luminescence from the Eu^{3+} ion in D4d symmetry, Inorg. Chim. Acta, 142 (1988), pp. 153-154, 10.1016/S0020-1693(00)80674-X.
7. R.A. Sá Ferreira, S.S. Nobre, C.M. Granadeiro, H.I.S. Nogueira, L.D. Carlos, O.L. Malta, A theoretical interpretation of the abnormal $^5D_0 \rightarrow {}^7F_4$ intensity based on the Eu^{3+} local coordination in the $Na_9[EuW_{10}O_{36}] \cdot 14H_2O$ polyoxometalate, J. Lumin., 121 (2006), pp. 561-567, 10.1016/j.jlumin.2005.12.044
8. OSRAM, LB QH9G Chip LED 0402 Datasheet, (n.d.). https://look.ams-osram.com/m/3184c82bafe7f3ef/original/LB-QH9G.pdf.
9. XLamp, XLAMP® WHITE LEDs, (n.d.). https://downloads.cree-led.com/files/fs/XLamp-Discrete-Directional-Feature-Sheet.pdf.
10. Y. Liu, J. Zhang, C. Zhang, J. Xu, G. Liu, J. Jiang, H. Jiang, $Ba_9Lu_2Si_6O_{24}:Ce^{3+}$: an efficient green phosphor with high thermal and radiation stability for solid-state lighting, Adv. Opt. Mater., 3 (2015), pp. 1096-1101, 10.1002/adom.201500078
11. B.R. Judd, Optical absorption intensities of rare-Earth ions, Phys. Rev., 127 (1962), pp. 750-761, 10.1103/PhysRev.127.750
12. G.S. Ofelt, Intensities of crystal spectra of rare-Earth ions, J. Chem. Phys., 37 (1962), pp. 511-520, 10.1063/1.1701366
13. M.P. Hehlen, M.G. Brik, K.W. Krämer, 50th anniversary of the Judd–Ofelt theory: an experimentalist's view of the formalism and its application, J. Lumin., 136 (2013), pp. 221-239, 10.1016/j.jlumin.2012.10.035
14. K. Binnemans, Interpretation of europium(III) spectra, Coord. Chem. Rev., 295 (2015), pp. 1-45, 10.1016/j.ccr.2015.02.015

15. B.M. Walsh, Judd-Ofelt theory: principles and practices, Adv. Spectrosc. Lasers Sens., Springer Netherlands, Dordrecht (2006), pp. 403-433, 10.1007/1-4020-4789-4_21
16. C.M. Dodson, R. Zia, Magnetic dipole and electric quadrupole transitions in the trivalent lanthanide series: Calculated emission rates and oscillator strengths, Phys. Rev. B, 86 (2012), Article 125102, 10.1103/PhysRevB.86.125102
17. C. Görller-Walrand, L. Fluyt, A. Ceulemans, W.T. Carnall, Magnetic dipole transitions as standards for Judd–Ofelt parametrization in lanthanide spectra, J. Chem. Phys., 95 (1991), pp. 3099-3106, 10.1063/1.460867
18. P.A. Tanner, Some misconceptions concerning the electronic spectra of tri-positive europium and cerium, Chem. Soc. Rev., 42 (2013), p. 5090, 10.1039/c3cs60033e
19. A. Ćirić, Ł. Marciniak, M.D. Dramićanin, Self-referenced method for the Judd–Ofelt parametrisation of the Eu3+ excitation spectrum, Sci. Rep., 12 (2022), p. 563, 10.1038/s41598-021-04651-4
20. A. Ćirić, S. Stojadinović, M. Sekulić, M.D. Dramićanin, JOES: an application software for Judd-Ofelt analysis from Eu3+ emission spectra, J. Lumin., 205 (2019), pp. 351-356, 10.1016/j.jlumin.2018.09.048
21. Komuro, N. et al. Synthesis, structure and optical properties of europium doped calcium barium phosphate – a novel phosphor for solid-state lighting. J. Mater. Chem. C 2, 6084–6089, https://doi.org/10.1039/c4tc00732h (2014).
22. Lachwa, H. & Reinen, D. Color and electronic structure of manganese(V) and manganese(VI) in tetrahedral oxo coordination. A spectroscopic investigation. Inorg. Chem. 28, 1044–1053, https://doi.org/10.1021/ic00305a011 (1989).
23. McCumber, D. E. & Sturge, M. D. Linewidth and temperature shift of the R lines in ruby. J. Appl. Phys. 34, 1682–1684, https://doi.org/10.1063/1.1702657 (1963)
24. Yen, W. M., Scott, W. C. & Schawlow, A. L. Phonon-induced relaxation in excited optical states of trivalent praseodymium in LaF₃. Phys. Rev. J. Archive 136, A271–A283, https://doi.org/10.1103/PhysRev.136.A271 (1964).
25. Pust, P. et al. Narrow-band red-emitting Sr[LiAl₃N₄]:Eu²⁺ as a next-generation LED-phosphor material. Nat. Mater. 13, 891–896, https://doi.org/10.1038/nmat4012 (2014).
26. Cao, R. P. et al. Near-infrared emission Ba₃(PO₄)₂:Mn⁵⁺ phosphor and potential application in vivo fluorescence imaging. Spectrochimica Acta Part A 128, 671–673, https://doi.org/10.1016/j.saa.2014.02.081 (2014)
27. Tanabe, Y. & Sugano, S. On the absorption spectra of complex ions. I. J. Phys. Soc. Jpn 9, 753–766, https://doi.org/10.1143/JPSJ.9.753 (1954).
28. Sugano, S., Tanabe, Y. & Kamimura, H. Multiplets of transition-metal ions in crystals (New York: Academic Press, 1970).
29. Brik, M. G. et al. Spin-forbidden transitions in the spectra of transition metal ions and nephelauxetic effect. ECS J. Solid State Sci. Technol. 5, R3067–R3077, https://doi.org/10.1149/2.0091601jss (2016).
30. Gschwend, P. M. et al. Simultaneous nanothermometry and deep-tissue imaging. Adv. Sci. 7, 2000370, https://doi.org/10.1002/advs.202000370 (2020).
31. Shen, Y. L. et al. Ag₂S nanoheaters with multiparameter sensing for reliable thermal feedback during in vivo tumor therapy. Adv. Funct. Mater. 30, 2002730, https://doi.org/10.1002/adfm.202002730 (2020).
32. Brik, M. G. et al. Crystal field parameters and energy level structure of the MnO₄³⁻ tetroxo anion in Li₃PO₄, Ca₂PO₄Cl and Sr₅(PO₄)₃Cl crystals. J. Luminescence 129, 801–806, https://doi.org/10.1016/j.jlumin.2009.02.018 (2009).
33. Shen, Y. R., Riedener, T. & Bray, K. L. Effect of pressure on site-symmetry distortions of Mn⁵⁺ and Cr⁴⁺ in Y₂SiO₅. Phys. Rev. B 61, 9277–9286, https://doi.org/10.1103/PhysRevB.61.9277 (2000).
34. Brik, M. G. et al. Spectroscopic and crystal field studies of YAlO₃ single crystals doped with Mn ions. J. Phys. Condensed Matter 21, 025404, https://doi.org/10.1088/0953-8984/21/2/025404 (2009).
35. Scott, M. A. et al. Optical spectroscopy of (MnO₄)³⁻ and (VO₄)⁵⁻ in Sr₁₀(VO₄)₆F₂. J. Phys. Condensed Matter 9, 9893–9908, https://doi.org/10.1088/0953-8984/9/45/017 (1997).
36. Andreici, E. L. Modeling of crystal field and spin-hamiltonian parameters for tetrahedral coordinated Mn⁵⁺ doped In Li₃VO₄. AIP Conf. Proc. 1472, 101–107, https://doi.org/10.1063/1.4748075 (2012).
37. V. Muhr, M. Buchnera, T. Hirsch, D.J. Jovanović, S.D. Dolić, M.D. Dramićanin, O.S. Wolfbeis, ens.

Actuator B Chem. 241 (2017) 349–356.

38. B. del Rosal, A. Pérez-Delgado, M. Misiak, A. Bednarkiewicz, A. S. Vanetsev, Y. Orlovskii, D. J. Jovanović, M. D. Dramićanin, U. Rocha, K. U. Kumar, C. Jacinto, E. Navarro, E.M. Rodriguez, M. Pedroni, A. Speghini. G.A. Hirata, I.R. Martin, D. Jacque, J. Appl. Phys. 118 (2015) 143104–143114.

39. L. Labrador-Páez, D.J. Jovanović, M.I. Marqués, K. Smits, S.D. Dolić, F. Jaque, H.E. Stanley, M.D. Dramićanin, J. García-Solé, P. Haro-González, D. Jaque, Small 13 (2017) 1700968.